

FIRST-YEAR *WILKINSON MICROWAVE ANISOTROPY PROBE (WMAP)*¹ OBSERVATIONS: PRELIMINARY MAPS AND BASIC RESULTS

C. L. BENNETT,² M. HALPERN,³ G. HINSHAW,² N. JAROSIK,⁴ A. KOGUT,² M. LIMON,^{2,5} S. S. MEYER,⁶ L. PAGE,⁴
D. N. SPERGEL,⁷ G. S. TUCKER,^{2,5,8} E. WOLLACK,² E. L. WRIGHT,⁹ C. BARNES,⁴ M. R. GREASON,¹⁰
R. S. HILL,¹⁰ E. KOMATSU,⁷ M. R. NOLTA,⁴ N. ODEGARD,¹⁰ H. V. PEIRIS,⁷
L. VERDE,⁷ AND J. L. WEILAND¹⁰

Received 2003 February 11; accepted 2003 May 29

ABSTRACT

We present full-sky microwave maps in five frequency bands (23–94 GHz) from the *Wilkinson Microwave Anisotropy Probe (WMAP)* first-year sky survey. Calibration errors are less than 0.5%, and the low systematic error level is well specified. The cosmic microwave background (CMB) is separated from the foregrounds using multifrequency data. The sky maps are consistent with the 7° FWHM *Cosmic Background Explorer (COBE)* maps. We report more precise, but consistent, dipole and quadrupole values. The CMB anisotropy obeys Gaussian statistics with $-58 < f_{\text{NL}} < 134$ (95% confidence level [CL]). The $2 \leq \ell \leq 900$ anisotropy power spectrum is cosmic-variance-limited for $\ell < 354$, with a signal-to-noise ratio greater than 1 per mode to $\ell = 658$. The temperature-polarization cross-power spectrum reveals both acoustic features and a large-angle correlation from reionization. The optical depth of reionization is $\tau = 0.17 \pm 0.04$, which implies a reionization epoch of $t_r = 180_{-80}^{+220}$ Myr (95% CL) after the big bang at a redshift of $z_r = 20_{-9}^{+10}$ (95% CL) for a range of ionization scenarios. This early reionization is incompatible with the presence of a significant warm dark matter density.

A best-fit cosmological model to the CMB and other measures of large-scale structure works remarkably well with only a few parameters. The age of the best-fit universe is $t_0 = 13.7 \pm 0.2$ Gyr. Decoupling was $t_{\text{dec}} = 379_{-7}^{+8}$ kyr after the big bang at a redshift of $z_{\text{dec}} = 1089 \pm 1$. The thickness of the decoupling surface was $\Delta z_{\text{dec}} = 195 \pm 2$. The matter density of the universe is $\Omega_m h^2 = 0.135_{-0.009}^{+0.008}$, the baryon density is $\Omega_b h^2 = 0.0224 \pm 0.0009$, and the total mass-energy of the universe is $\Omega_{\text{tot}} = 1.02 \pm 0.02$. It appears that there may be progressively less fluctuation power on smaller scales, from *WMAP* to fine-scale CMB measurements to galaxies and finally to the Ly α forest. This may be accounted for with a running spectral index of scalar fluctuations, fitted as $n_s = 0.93 \pm 0.03$ at wavenumber $k_0 = 0.05 \text{ Mpc}^{-1}$ ($\ell_{\text{eff}} \approx 700$), with a slope of $dn_s/d \ln k = -0.031_{-0.018}^{+0.016}$ in the best-fit model. (For *WMAP* data alone, $n_s = 0.99 \pm 0.04$.) This flat universe model is composed of 4.4% baryons, 22% dark matter, and 73% dark energy. The dark energy equation of state is limited to $w < -0.78$ (95% CL). Inflation theory is supported with $n_s \approx 1$, $\Omega_{\text{tot}} \approx 1$, Gaussian random phases of the CMB anisotropy, and superhorizon fluctuations implied by the temperature-polarization anticorrelations at decoupling. An admixture of isocurvature modes does not improve the fit. The tensor-to-scalar ratio is $r(k_0 = 0.002 \text{ Mpc}^{-1}) < 0.90$ (95% CL). The lack of CMB fluctuation power on the largest angular scales reported by *COBE* and confirmed by *WMAP* is intriguing. *WMAP* continues to operate, so results will improve.

Subject headings: cosmic microwave background — cosmology: observations — dark matter — early universe — instrumentation: detectors — space vehicles: instruments

1. INTRODUCTION

The cosmic microwave background (CMB) radiation was first detected by Penzias & Wilson (1965). After its discovery, a small number of experimentalists worked for years to better characterize the CMB as they searched for

temperature fluctuations. A leader of this effort, and of the *Wilkinson Microwave Anisotropy Probe (WMAP)* effort, was our recently deceased colleague, Professor David T. Wilkinson of Princeton University. He was also a leading member of the *Cosmic Background Explorer (COBE)* mission team, which accurately characterized the spectrum of

¹ *WMAP* is the result of a partnership between Princeton University and the NASA Goddard Space Flight Center. Scientific guidance is provided by the *WMAP* Science Team.

² NASA Goddard Space Flight Center, Code 685, Greenbelt, MD 20771; charles.l.bennett@nasa.gov.

³ Department of Physics and Astronomy, University of British Columbia, Vancouver, BC V6T 1Z1, Canada.

⁴ Department of Physics, Jadwin Hall, Princeton, NJ 08544.

⁵ National Research Council Fellow.

⁶ Departments of Astrophysics and Physics, EFI, and CfCP, University of Chicago, Chicago, IL 60637.

⁷ Department of Astrophysical Sciences, Princeton University, Princeton, NJ 08544.

⁸ Department of Physics, Brown University, Providence, RI 02912.

⁹ Department of Astronomy, UCLA, P.O. Box 951562, Los Angeles, CA 90095-1562.

¹⁰ Science Systems and Applications, Inc. (SSAI), 10210 Greenbelt Road, Suite 600, Lanham, MD 20706.

the CMB (Mather et al. 1990, 1999) and first discovered anisotropy (Smoot et al. 1992; Bennett et al. 1992; Kogut et al. 1992; Wright et al. 1992). The *MAP* was recently renamed *WMAP* in his honor.

The general recognition that the CMB is a primary tool for determining the global properties, content, and history of the universe has led to the tremendous interest and growth of the field. In addition to the characterization of the large-scale anisotropy results from *COBE* (Bennett et al. 1996; Hinshaw et al. 1996a, 1996b; Kogut et al. 1996a, 1996b, 1996c; Górski et al. 1996; Wright et al. 1996a), a host of experiments have measured the finer scale anisotropy (Benoit et al. 2003; Grainge et al. 2003; Pearson et al. 2003; Ruhl et al. 2003; Kuo et al. 2002; Dawson et al. 2001; Halverson et al. 2002; Hanany et al. 2000; Leitch et al. 2000; Wilson et al. 2000; Padin et al. 2001; Romeo et al. 2001; Harrison et al. 2000; Peterson et al. 2000; Baker et al. 1999; Coble et al. 1999; Dicker et al. 1999; Miller et al. 1999; de Oliveira-Costa et al. 1998; Cheng et al. 1997; Hancock et al. 1997; Netterfield et al. 1997; Piccirillo et al. 1997; Tucker et al. 1997; Gundersen et al. 1995; de Bernardis et al. 1994; Ganga et al. 1993; Myers, Readhead, & Lawrence 1993; Tucker et al. 1993). As a result of these tremendous efforts, the first acoustic peak of the anisotropy power spectrum has been unambiguously detected (Knox & Page 2000; Mautkopf et al. 2000; Miller et al. 1999), and CMB observations have placed important constraints on cosmological models. Recently, Kovac et al. (2002) reported the first detection of CMB polarization arising from the anisotropic scattering of CMB photons at decoupling, ushering in a new era of CMB polarization measurements.

The *WMAP* mission was designed to advance observational cosmology by making full-sky CMB maps with accuracy, precision, and reliability, as described by Bennett et al. (2003a). The instrument observes the temperature difference between two directions (as did *COBE*) using two nearly identical sets of optics (Page et al. 2003a, 2003b). These optics focus radiation into horns (Barnes et al. 2002) that feed differential microwave radiometers (Jarosik et al. 2003a). We produce full-sky maps in five frequency bands from the radiometer data of temperature differences measured over the full sky. A CMB map is the most compact representation of CMB anisotropy without loss of information.

In this paper we present the maps, their properties, and a synopsis of the basic results of the first year of observations. In § 2 we give a brief overview of the *WMAP* mission. In § 3 we summarize the data analysis, calibration, and systematic errors of the experiment, which are discussed in much greater detail in the companion papers by Hinshaw et al.

(2003a), Page et al. (2003b), Jarosik et al. (2003b), and Barnes et al. (2003). In § 4 we present the maps and their sampling properties, and we compare the *WMAP* and *COBE* maps. In § 5 we summarize the foreground analyses of Bennett et al. (2003a). In § 6 we establish the Gaussian nature of the *WMAP* anisotropy, determined in the companion paper of Komatsu et al. (2003). In § 7 we present the dipole and quadrupole moments and summarize analyses of the angular power spectrum (Hinshaw et al. 2003b; Verde et al. 2003). In § 8 we highlight the *WMAP* polarization results, including a detection of the reionization of the universe (Kogut et al. 2003). In § 9 we summarize some of the cosmological implications of the *WMAP* results (Page et al. 2003a; Spergel et al. 2003; Peiris et al. 2003). Finally, in § 10 we discuss the availability of the *WMAP* data products.

2. OBSERVATIONS

The 840 kg *WMAP* observatory was launched aboard a Delta II 7425-10 rocket (Delta launch number 286) on 2001 June 30 at 3:46:46.183 EDT from Cape Canaveral. *WMAP* executed three phasing loops in the Earth-Moon system before a lunar-gravity-assist swing-by, a month after launch, catapulted *WMAP* to an orbit at about the second Lagrange point of the Sun-Earth system, L2. Station-keeping is performed approximately four times per year to maintain the observatory in a Lissajous orbit about the L2 point with the Earth-*WMAP* vector within $\sim 1^\circ$ – 10° of the Sun-Earth vector. The phasing loop maneuvers and station-keeping are executed using the *WMAP* propulsion system of blow-down hydrazine and eight thrusters.

The central design philosophy of the *WMAP* mission was to minimize sources of systematic measurement errors (Bennett et al. 2003a). The *COBE* mission proved the effectiveness of a differential design in minimizing systematic errors. Therefore, the *WMAP* instrument was designed with a back-to-back optical system with $1.4 \text{ m} \times 1.6 \text{ m}$ primary reflectors to provide for differential measurements of the sky. The primary and secondary reflectors direct radiation into two focal planes, with 10 feed horns in each, as described by Page et al. (2003a).

The beams have a gain pattern G , which is neither symmetric nor Gaussian. We define the beam solid angle as $\int [G(\Omega)/G_{\text{max}}] d\Omega$. The beam size can be expressed as the square root of the beam solid angles, giving $0^\circ 22$, $0^\circ 35$, $0^\circ 51$, $0^\circ 66$, and $0^\circ 88$ for the W band through the K band, respectively. Alternately, the beams can be expressed in terms of a FWHM for each band, given in Table 1. Detailed analyses of the *WMAP* beams are discussed by Page et al. (2003a, 2003b).

TABLE 1
APPROXIMATE OBSERVATIONAL PROPERTIES BY BAND

Item	K Band	Ka Band	Q Band	V Band	W Band
Wavelength, λ (mm).....	13	9.1	7.3	4.9	3.2
Frequency, ν (GHz).....	22.8	33.0	40.7	60.8	93.5
Ant./therm. conversion factor, $\Delta T/\Delta T_A$	1.014	1.029	1.044	1.100	1.251
Noise, σ_0 (mK), $\sigma = \sigma_0 N_{\text{obs}}^{-1/2}$	1.424	1.449	2.211	3.112	6.498
Beam width θ (deg FWHM).....	0.82	0.62	0.49	0.33	0.21
Number of differencing assemblies.....	1	1	2	2	4
Number of radiometers.....	2	2	4	4	8
Number of channels.....	4	4	8	8	16

The feed horns are attached to orthomode transducers (OMTs) that split the polarization of the incoming signal into a differential correlation radiometer system with High Electron Mobility Transistor (HEMT) amplifiers. There are 10 “differencing assemblies,” each consisting of two “radiometers” with two “channels” each (Jarosik et al. 2003a; Bennett et al. 2003a). There are four W-band (~ 94 GHz), two V-band (~ 61 GHz), two Q-band (~ 41 GHz), one Ka-band (~ 33 GHz), and one K-band (~ 23 GHz) differencing assemblies. We usually refer to these bands by the generic designations K, Ka, Q, V, and W because there are multiple radiometers in each band, whose precise frequencies are not identical. In addition, the effective frequency of a radiometer depends on the spectrum of the emission it detects. Precise frequencies for the radiometers for a CMB anisotropy spectrum are given by Jarosik et al. (2003a). Polynomials are given to determine the effective frequency of the radiometers depending on the emission frequency spectrum. See Table 1 for a summary of radiometer properties.

Undesirable $1/f$ noise is minimized by the design of the *WMAP* radiometers (Jarosik et al. 2003a). All radiometers have $1/f$ knees below 50 mHz; 18 of 20 are below 10 mHz, and 10 of the 20 are below 1 mHz (Jarosik et al. 2003b). (The $1/f$ knee is defined as the frequency at which the noise power spectral density is $\sqrt{2}$ times higher than its high-frequency value.) Jarosik et al. (2003a) demonstrate that all radiometer outputs have Gaussian noise, which “integrates down” with time as expected.

The radiometers are passively cooled to ~ 90 K with no mechanical refrigerators. In addition, no actively cycling heaters were permitted anywhere on the *WMAP* spacecraft. These design features helped to ensure a mechanically, thermally, and electronically quiet platform that minimizes the driving forces of systematic measurement errors.

In addition to the differential design, the *COBE* mission also demonstrated the importance of scanning large areas of the sky in a short period of time with a complex scan pattern. *WMAP* follows the *COBE* example with a three-axis (three reaction wheel) control system that maintains the observatory in a nearly constant survey mode of operations. (The observatory is in constant survey mode, except for only ~ 1 hr for each of approximately four station-keeping maneuvers per year.) In survey mode, the optical boresight sweeps out a complex pattern on the sky (Bennett et al. 2003a). Approximately 30% of the sky is observed each hour. The observatory spins at 0.464 rpm (~ 7.57 mHz) and precesses at 1 revolution hr^{-1} (~ 0.3 mHz).

Six months are required for L2 to orbit half-way around the Sun, allowing for full-sky coverage. The observations presented in this and companion papers include a full orbit about the Sun, thus containing two sets of full-sky observa-

tions. By 2001 August 10, *WMAP* was sufficiently stable in its L2 orbit for CMB data taking to commence. One year of observations, completed on 2002 August 9, were analyzed. Data taken beyond this date will be the subject of future analyses.

3. DATA PROCESSING, CALIBRATION, AND SYSTEMATIC ERRORS

Time-ordered telemetry data from the observatory are downlinked via NASA’s Deep Space Network to the *WMAP* Science and Mission Operations Center (SMOC) at the Goddard Space Flight Center. The data are then transferred to the *WMAP* Science Team for analysis. All of the instrument data are downlinked to the ground without any onboard flight data processing, thus allowing full insight into potential systematic effects.

Only a fraction of a percent of data were lost in the flow from the observatory to the SMOC. About 1% of the received data were not used because of systematic error concerns (e.g., data taken during or near station-keeping maneuvers). Of the $\sim 99\%$ good data, the processing pipeline flagged observations where bright planets were in the beams so that these data would not be used in making maps. The statistics on lost, bad, and flagged data are given in Table 2.

An overview of the data flow is shown in Figure 1. The heart of the data analysis efforts centers on studies of systematic measurement errors (Hinshaw et al. 2003b). Components of spurious signals at the spin period are the most difficult to distinguish from true sky signals. The observatory was designed to minimize all thermal and voltage variations and all susceptibilities to these variations, especially at the spin period, as discussed in § 2 and by Bennett et al. (2003a). In addition, high-precision temperature monitors on the observatory provide the data needed to verify that systematic errors from thermal variations are negligible. Jarosik et al. (2003b) report that in-flight spin-synchronous effects from the radiometers are less than $0.17 \mu\text{K}$ rms in the time-ordered data (TOD), based on flight thermal variations multiplied by upper limits on component susceptibilities measured in ground testing. Analysis of flight data without use of characterizations derived from ground-based testing give less than $0.14 \mu\text{K}$ rms from all sources (not just the radiometers). This is a factor of more than 50 times smaller than the requirement that was set in the mission’s systematic error budget. Thus, *no corrections to the first-year WMAP data are required for spin-synchronous systematic errors.*

The core of the processing pipeline calibrates the data and converts the differential temperatures into maps. The

TABLE 2
DATA FLAGGING SUMMARY

Category	K Band	Ka Band	Q Band	V Band	W Band
Rejected or lost data:					
Lost data (%).....	0.27	0.27	0.27	0.27	0.27
Spacecraft thermal change (%).....	0.87	0.87	0.87	0.87	0.87
Gain or baseline step (%).....	0.00	0.13	0.12	0.00	0.22
Total lost or bad data (%).....	1.04	1.27	1.26	1.14	1.36
Data not used in maps:					
Planet flag (%).....	0.11	0.11	0.11	0.11	0.11

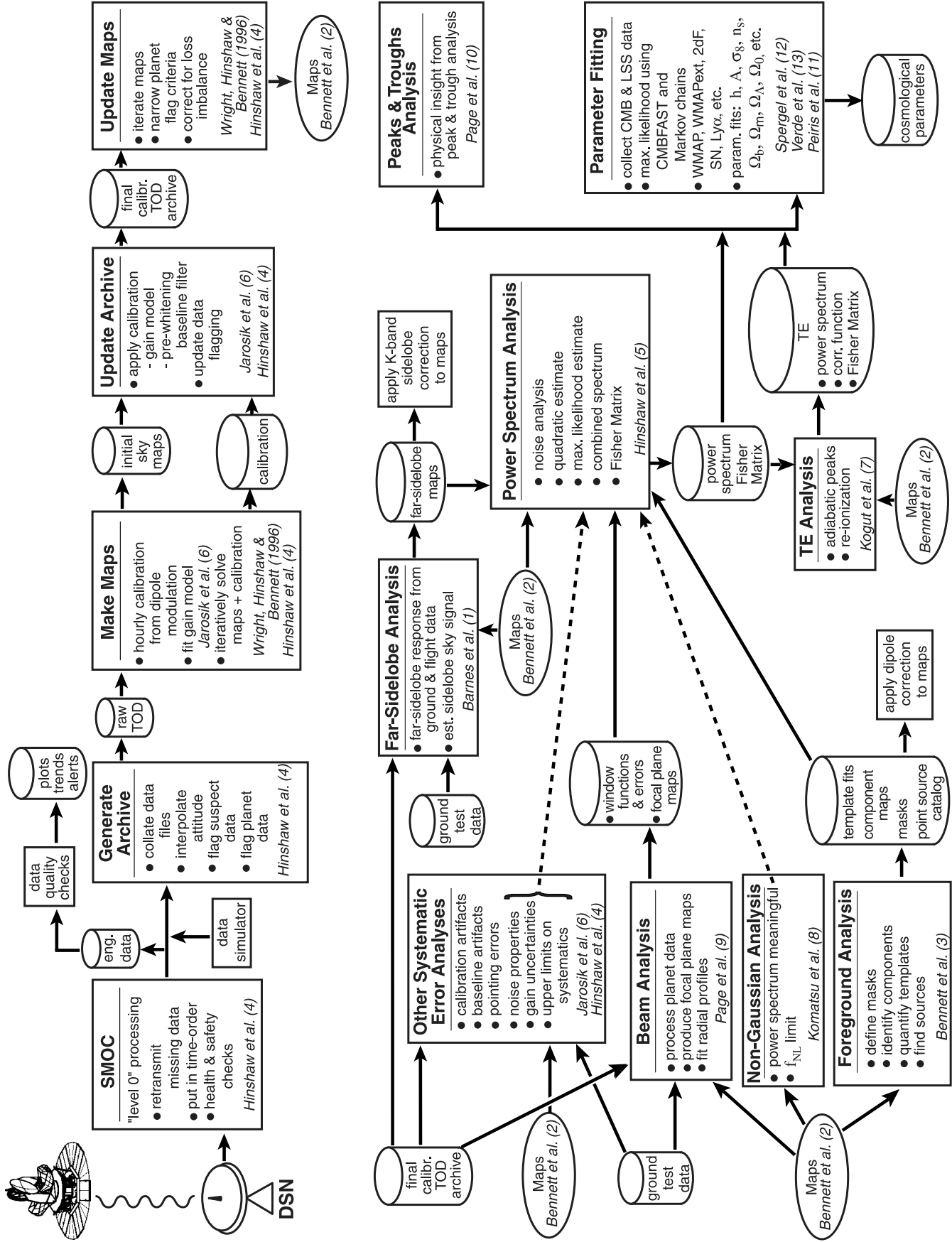


FIG. 1.—Overview of the WMAP data flow. References: (1) Barnes et al. 2003; (2) this paper; (3) Bennett et al. 2003b; (4) Hinshaw et al. 2003b; (5) Hinshaw et al. 2003b; (6) Jarosik et al. 2003b; (7) Kogut et al. 2003; (8) Komatsu et al. 2003; (9) Page et al. 2003b; (10) Page et al. 2003c; (11) Peiris et al. 2003; (12) Spergel et al. 2003; (13) Verde et al. 2003.

data are calibrated based on the Earth-velocity modulation of the CMB dipole. A gain model of the radiometers was derived and fitted by Jarosik et al. (2003b). The model is based on the constancy of the dipole signal on the sky, the measured physical temperature of the front-end radiometer components, and the time-averaged radio-frequency bias (total power) of the radiometer outputs. This relatively simple model closely matches the gains derived from the hourly measurements of the amplitude of the dipole and is used in *WMAP* data processing. Calibration is achieved within 0.5% accuracy, dominated by the statistical uncertainty in the absolute calibration.

Low levels of $1/f$ noise create stripes in the maps that affect the angular power spectrum and other statistics derived from the maps. A prewhitening filter is applied to the TOD to minimize these artifacts. An estimate of the magnitude of the striping is given by Hinshaw et al. (2003b) for the maps and by Hinshaw et al. (2003a) for the power spectrum.

The differential temperature data are formed into maps based on the technique introduced by Wright et al. (1996b). HEALPix¹¹ is used to define map pixels on the sky in Galactic coordinates. Various levels of resolution are specified by a “resolution level” with an integer ($r = 0, 1, 2, \dots$). With $N_{\text{side}} = 2^r$, the number of pixels in the map is $N_{\text{pix}} = 12N_{\text{side}}^2$. The area per pixel is $\Omega_{\text{pix}} = 4\pi/N_{\text{pix}}$, and the separation between pixel centers is $\theta_{\text{pix}} = \Omega_{\text{pix}}^{1/2}$. For example, HEALPix resolution level $r = 9$ (used in *WMAP* map-making) corresponds to $N_{\text{side}} = 512$, $N_{\text{pix}} = 3,145,728$, $\Omega_{\text{pix}} = 3.99 \times 10^{-6}$ sr, and $\theta_{\text{pix}} = 0.115 = 6.87'$.

WMAP observes the sky convolved with the beam pattern. This is equivalent to the spatial transform of the sky multiplied by the instrument’s “window function.” The beam patterns are measured in flight from observations of Jupiter (Page et al. 2003b). Uncertainties in our knowledge of the beam pattern, although small, are a significant source of uncertainty for *WMAP*, since they imply imperfect knowledge of the window function. A small difference between the A-side and B-side optical losses was derived based on dipole observations and corrected in the processing. Far sidelobes of the beam patterns, determined by ground measurements and in flight using the Moon, have been carefully examined (Barnes et al. 2003). A small far sidelobe correction is applied to only the K-band map. We now describe the maps.

4. THE MAPS

We combine the radiometer results within each band and present the five full-sky maps at effective CMB anisotropy frequencies of 23, 33, 41, 61, and 94 GHz in Figures 2a–2e. The maps are shown in the Mollweide projection in units of CMB thermodynamic temperature. The number of independent observations that contribute to each pixel forms the sky pattern in Figure 3. Figure 4 provides an overall guide to some of the more prominent features of the maps as well as point sources detected by *WMAP*, as described herein.

Figure 5 shows the K-band and Ka-band maps, with the Ka-band map smoothed to K-band resolution. Note both the significant decrease in Galactic signal from the K band

to the Ka band and the high Galactic latitude similarities of the CMB between the maps. Likewise, Figure 6 shows the Q-band, V-band, and W-band maps with the latter two smoothed to Q-band resolution. Higher Galactic contamination in the Q band is apparent. Both Figures 5 and 6 highlight the consistency of the high Galactic latitude CMB anisotropy pattern from band to band.

Comparisons of data between *WMAP* radiometers, and between *WMAP* and *COBE*, are important indicators of systematic error levels. Figure 7 illustrates the enormous improvement in angular resolution from *COBE* to *WMAP*. Features in the maps appear to be generally consistent, but the consistency is better addressed by a more direct comparison. To do this we take a combination of the *WMAP* Q-band and V-band maps and smooth it to mimic a *COBE* Differential Microwave Radiometer (DMR) 53 GHz map (see Fig. 8). We then examine the difference between the *COBE* map and *WMAP* pseudomap. Figure 9 shows the difference map along with a simulated map of the noise. With the exception of a feature in the Galactic plane, the agreement is clearly at the noise level. The Galactic plane feature is likely to be a result of the spectral index uncertainty of combining the Q-band and V-band maps to make a 53 GHz equivalent map.

5. FOREGROUND ANALYSES

An understanding of diffuse Galactic emission and extragalactic point sources is necessary for CMB analyses. The *WMAP* mission carries radiometers at five frequencies for the purpose of separating the CMB anisotropy from foreground emission based on their different spectra. Figure 10 illustrates the spectral difference between the CMB and foregrounds. The *WMAP* bands were selected to be near the frequency at which the ratio of the CMB anisotropy to the contaminating foreground is at a maximum.

5.1. Masks

For CMB analyses it is necessary to mask out regions of bright foreground emission. Bennett et al. (2003b) present a recipe for foreground masks based on K-band temperature levels. Since foreground contamination is most severe in the K-band, it is used as the best tracer of contamination. The contamination morphology is similar enough across all five *WMAP* bands that masks based on the temperature levels in other bands would be redundant and unnecessary. Standard names are given for the mask levels. For example, the Kp0 mask cuts 21.4% of sky pixels, while the Kp2 mask cuts 13.1%. See Bennett et al. (2003b) for further detail. An extragalactic point-source mask is also constructed based on selections from source catalogs. An additional 2% of pixels are masked because of these ~ 700 sources.

5.2. Diffuse Galactic Emission

Beyond the use of masks, one technique for reducing the level of foreground contamination is to form a linear combination of the multifrequency *WMAP* data that retains unity response for only the emission component with a CMB spectrum. This technique was introduced for *COBE* by Bennett et al. (1992). With five *WMAP* bands instead of the three on *COBE*, and with a somewhat more elaborate approach for *WMAP*, Bennett et al. (2003b) arrive at the internal (*WMAP* data only) linear combination map seen in

¹¹ See <http://www.eso.org/science/healpix>.

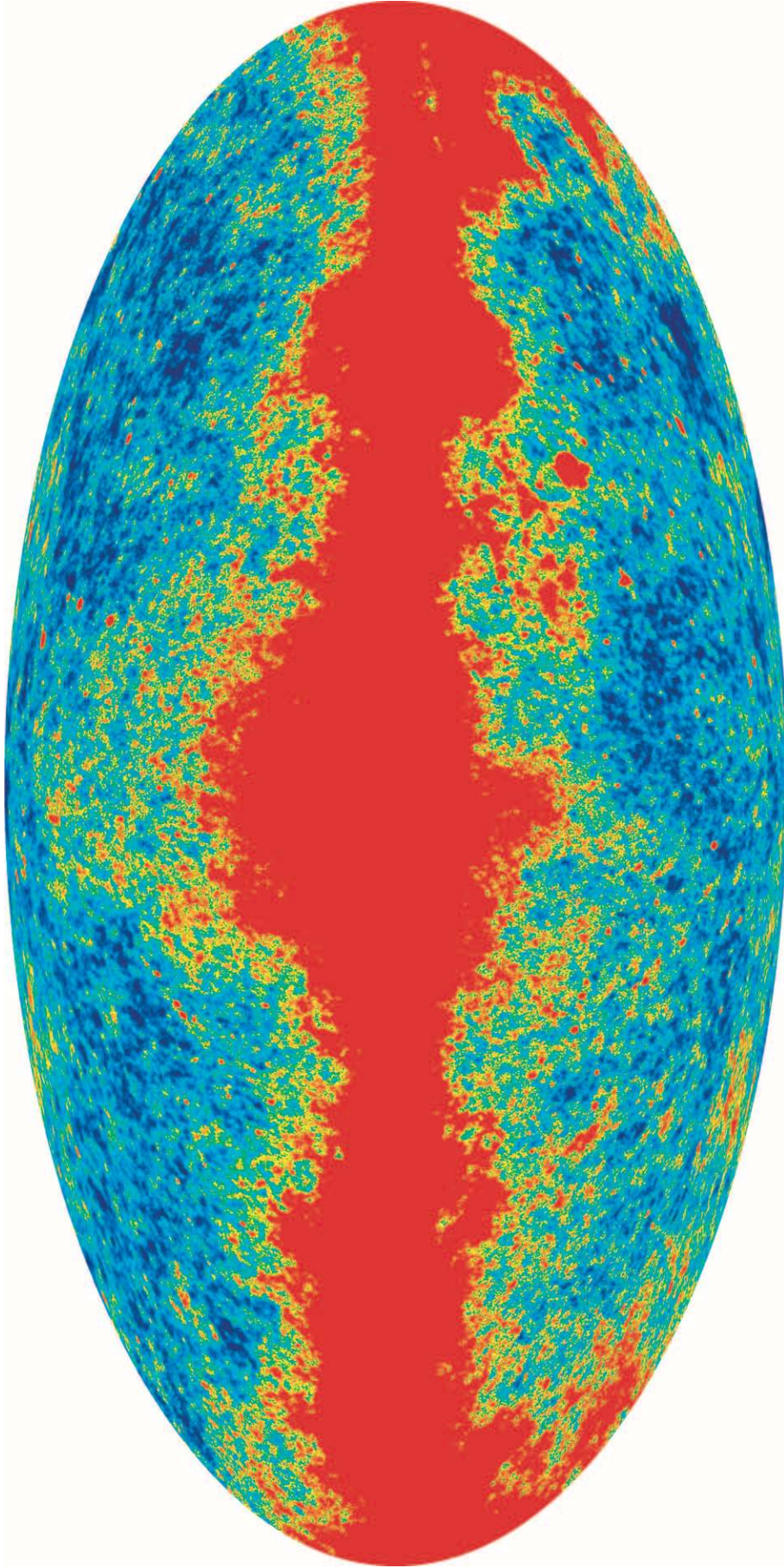


FIG. 2a

FIG. 2.— Full-sky maps in the five *WMAP* frequency bands, shown in a Mollweide projection in Galactic coordinates. (a) K band. (b) Ka band. (c) Q band. (d) V band. (e) W band.

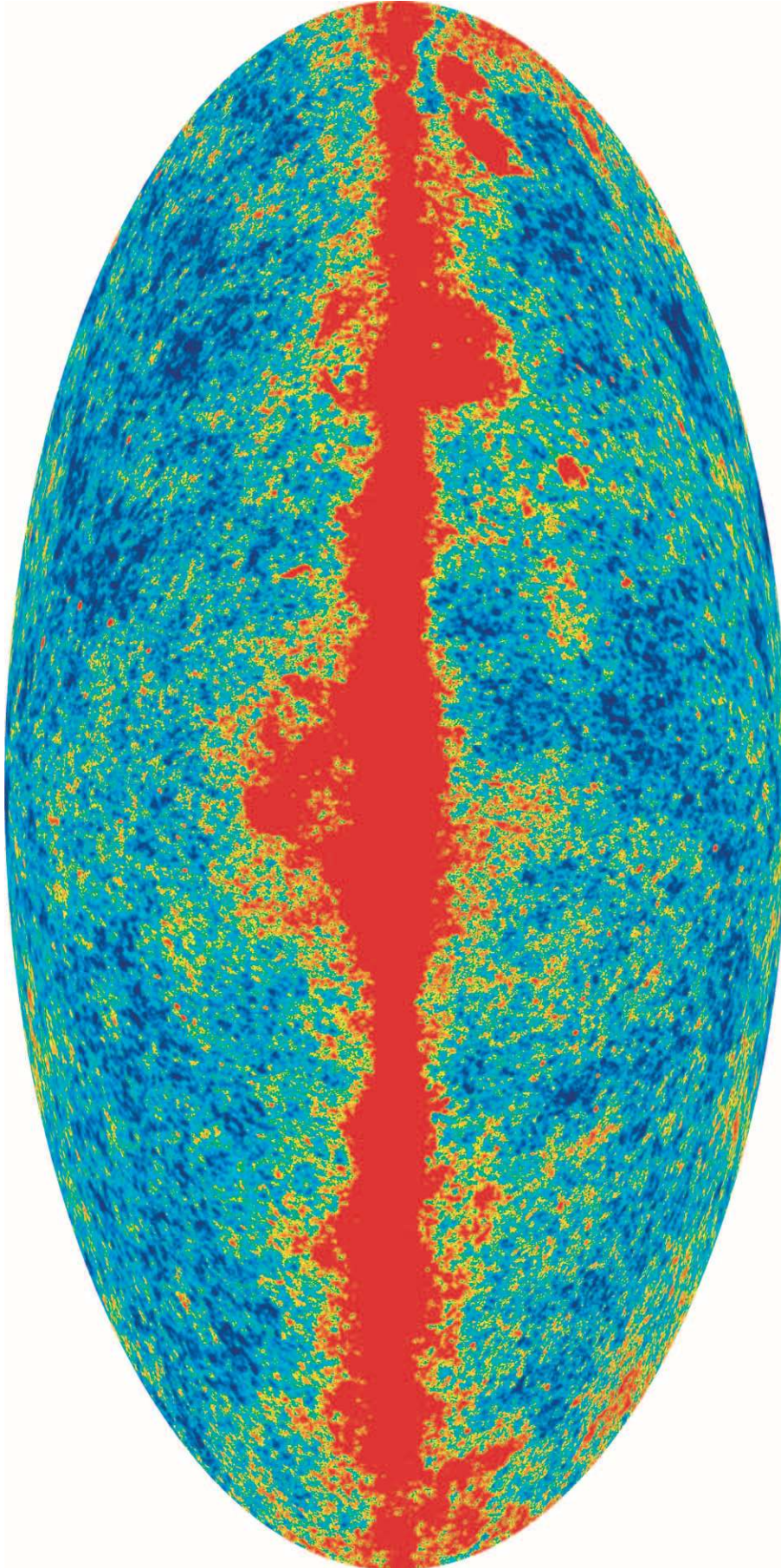
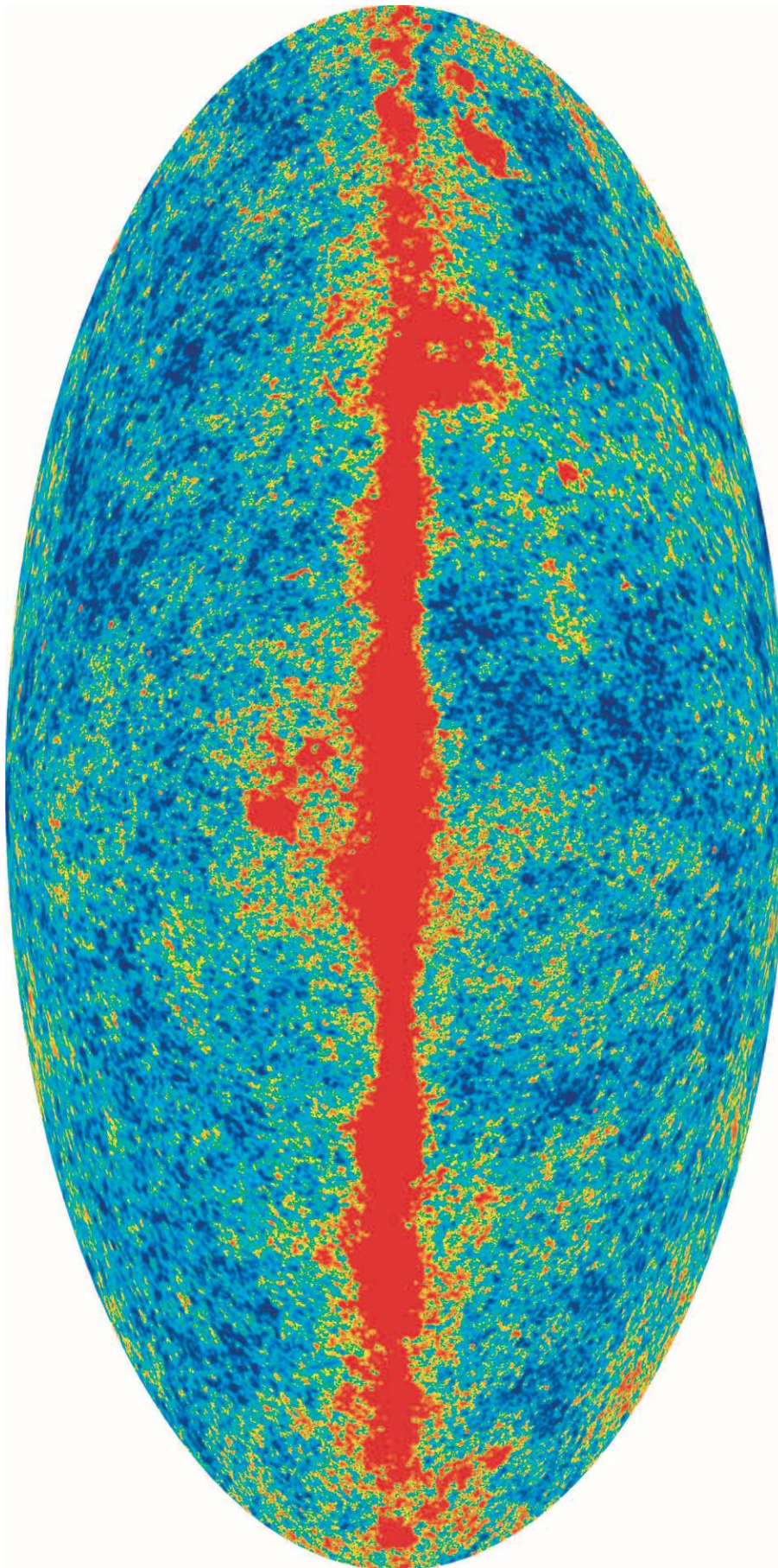


FIG. 24



T (μK)
-200 +200

FIG. 2c

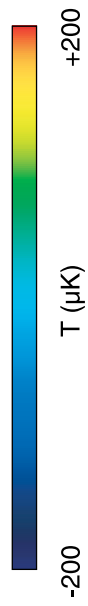
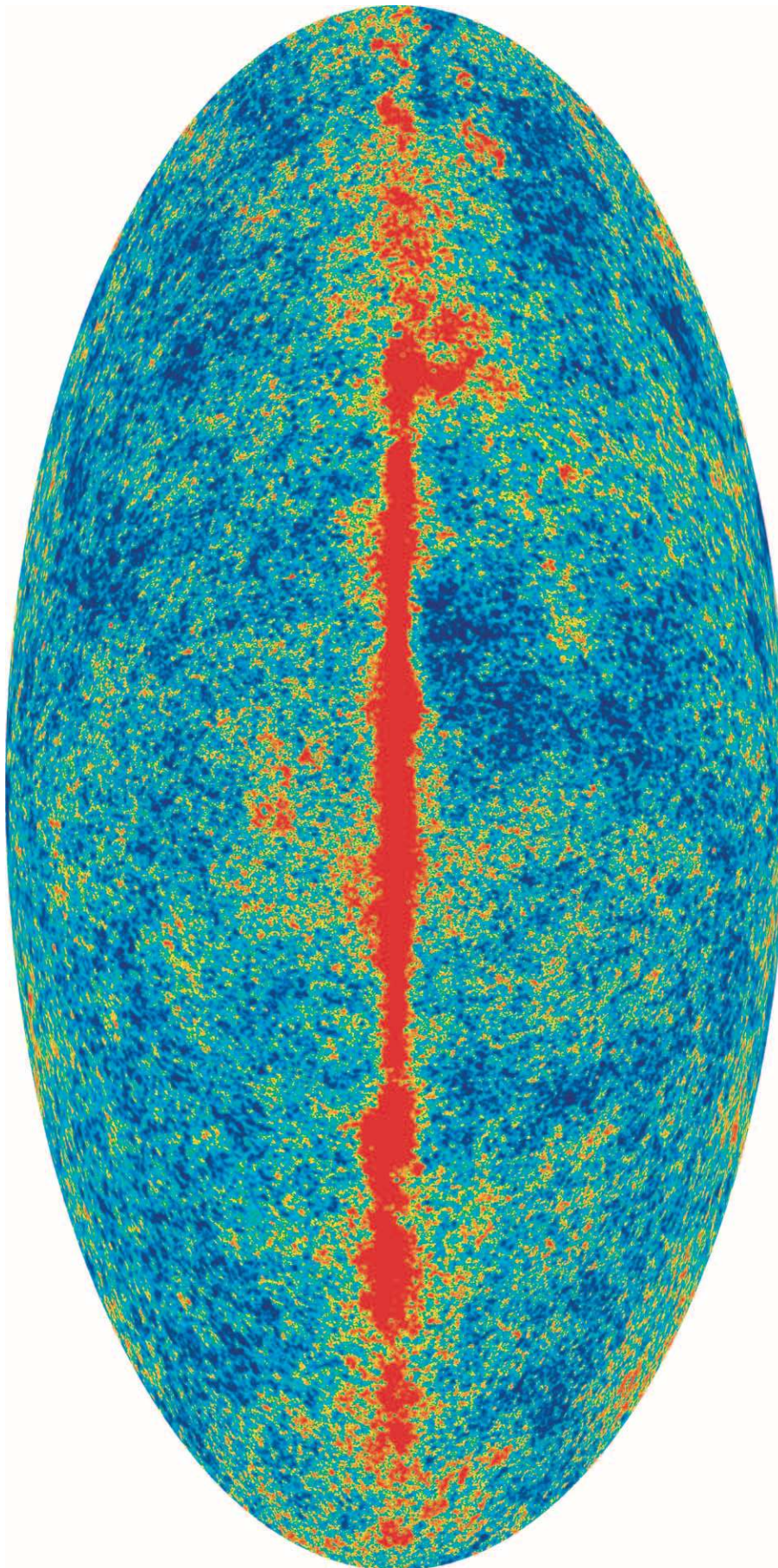
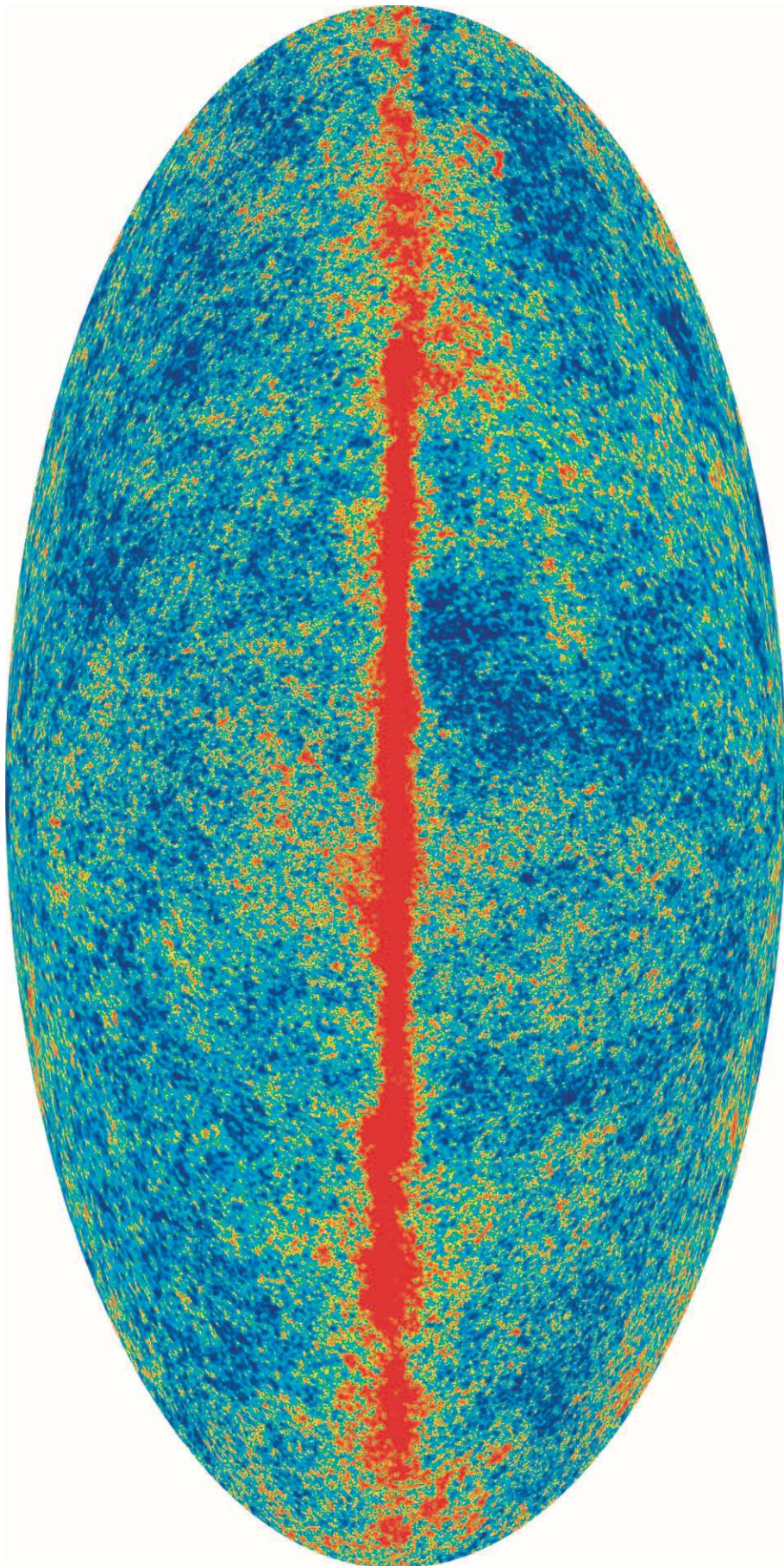


FIG. 2d



T (μK)

-200

+200

FIG. 2e

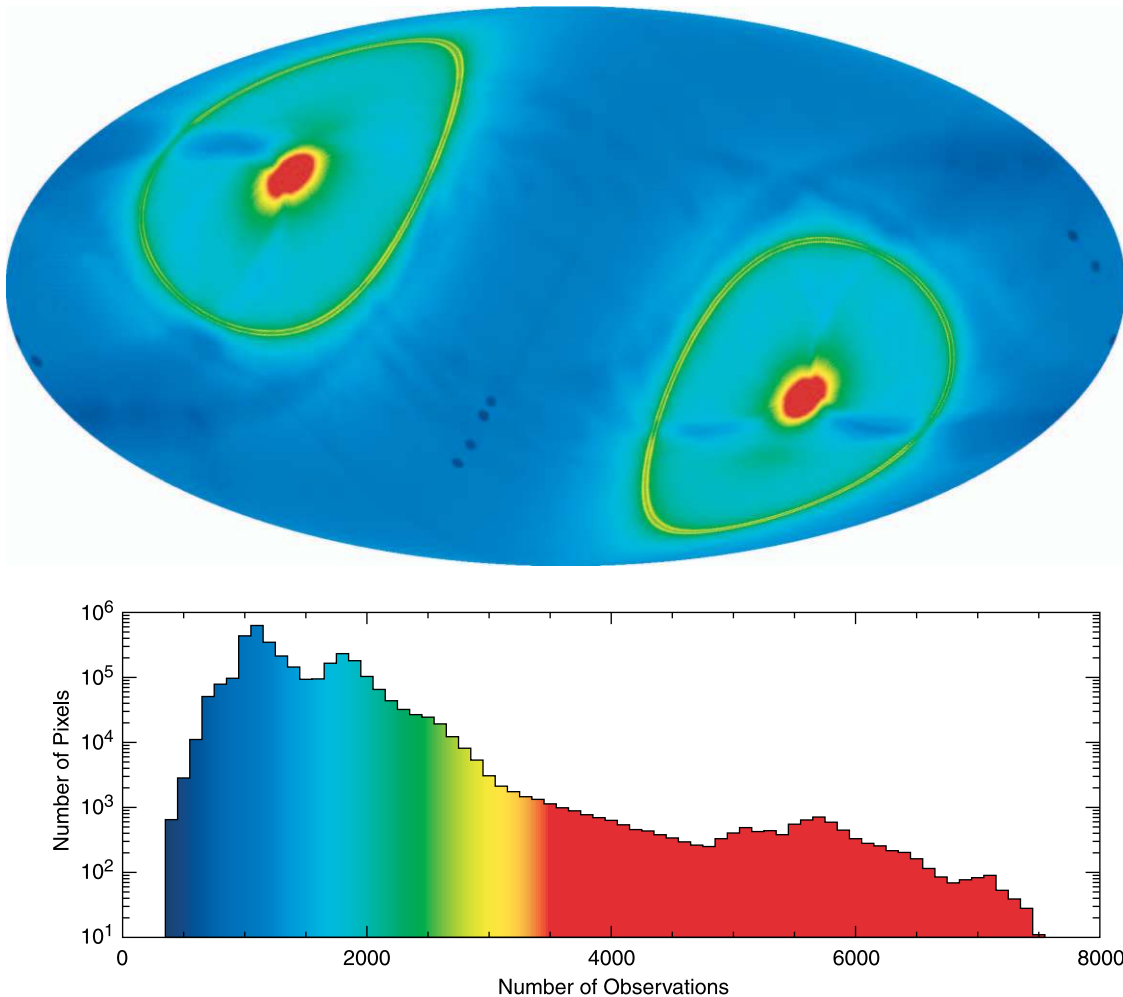


FIG. 3.—Number of independent observations per pixel in Galactic coordinates. The number of observations is greatest at the ecliptic poles and in rings around the ecliptic poles with diameters corresponding to the separation angle of the two optical boresight directions (approximately 141°). The observations are the most sparse in the ecliptic plane. Small area cuts are apparent where Mars, Saturn, Jupiter, Uranus, and Neptune data are masked so as not to contaminate CMB analyses. Jupiter data are used for beam mapping. The histogram of the sky sampling shows the departures from uniform sky coverage.

Figure 11 of this paper. The foregrounds are removed to a remarkable degree; however, the statistics of this internal linear combination map are complex and inappropriate for most CMB analyses.

Below, we use the notation convention that flux density is $S \sim \nu^\alpha$ and antenna temperature is $T_A \sim \nu^\beta$, where the spectral indexes are related by $\beta = \alpha - 2$. In general, the CMB is expressed in terms of thermodynamic temperature, while Galactic and extragalactic foregrounds are expressed in antenna temperature. Thermodynamic temperature differences are given by $\Delta T = \Delta T_A [(e^x - 1)^2 / x^2 e^x]$, where $x = h\nu/kT_0$, h is the Planck constant, ν is frequency, k is the Boltzmann constant, and $T_0 = 2.725$ K is the CMB temperature (Mather et al. 1999). Values of $\Delta T/\Delta T_A$ for the *WMAP* bands are given by Jarosik et al. (2003b) and can be found in Table 1.

Bennett et al. (2003b) identify the amplitudes and spectral indexes of the individual emission components. A maximum entropy method (MEM) approach is adopted in which priors are used for component amplitudes and spectral indexes, except for free-free emission, which has a fixed spectral index ($\beta = -2.15$ in the *WMAP* bands). An iterative fit is performed, in which the pixel-by-pixel amplitudes are updated

in accordance with the MEM residuals until low ($<1\%$) residuals are achieved. The process results in a map of each emission component for each of the five *WMAP* bands. The derived maps of thermal emission from dust give a uniform spectral index across the sky of $\beta_d \approx 2.2$. The derived map of free-free emission is reasonable given the amplitude and morphology of $H\alpha$ measurements. The other radio component fit should include the combined emission of synchrotron and spinning dust. It shows the synchrotron spectrum steepening with increasing frequency, as would be expected for a spectral break due to synchrotron losses at ≈ 20 GHz. There is no indication of the less steep or flattening spectral index that would result from spinning dust emission. The spinning dust emission is limited to less than 5% of the total Ka-band foreground. Reports of dust-correlated microwave emission from *COBE* data analyses are understood as an admixture of the fraction of synchrotron emission (with $\beta \approx -3$) that is traced by a dust template and thermal dust emission ($\beta \approx 2.2$), giving a combined spectral index of $\beta \approx -2.2$ between the *WMAP* Ka band and V band, approximating the *COBE* 31 and 53 GHz bands.

While the MEM is useful for understanding the nature of the foreground emission components, these results

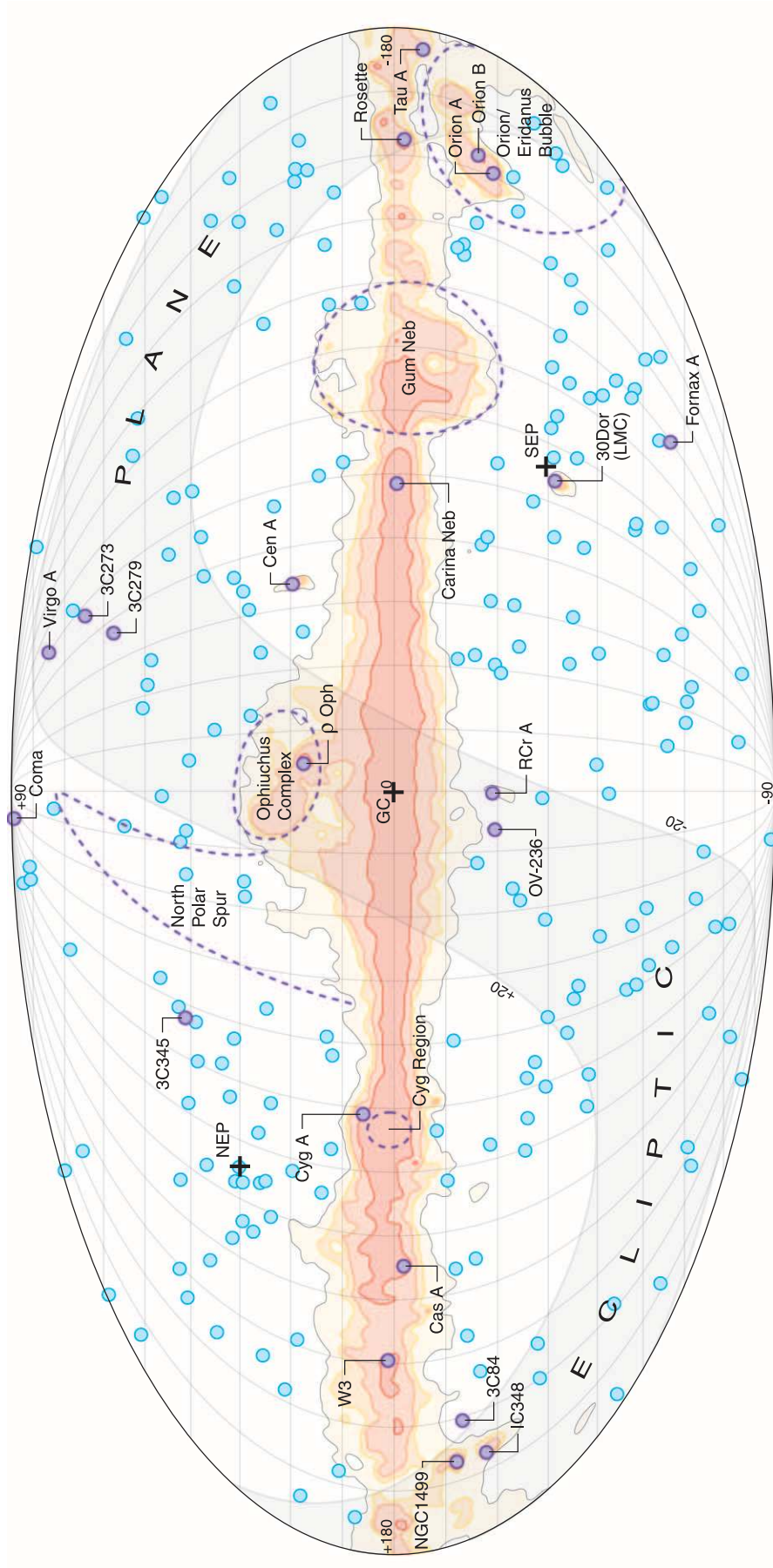


FIG. 4.—Guide to the microwave sky for reference. This picture shows the large-scale emission from the Milky Way, including some of its notable components such as the Cygnus complex, the north polar spur, the Gum region, etc. The small circles show positions of the microwave point sources detected by *WMAP* (Bennett et al. 2003b). The brighter sources are labeled for reference.

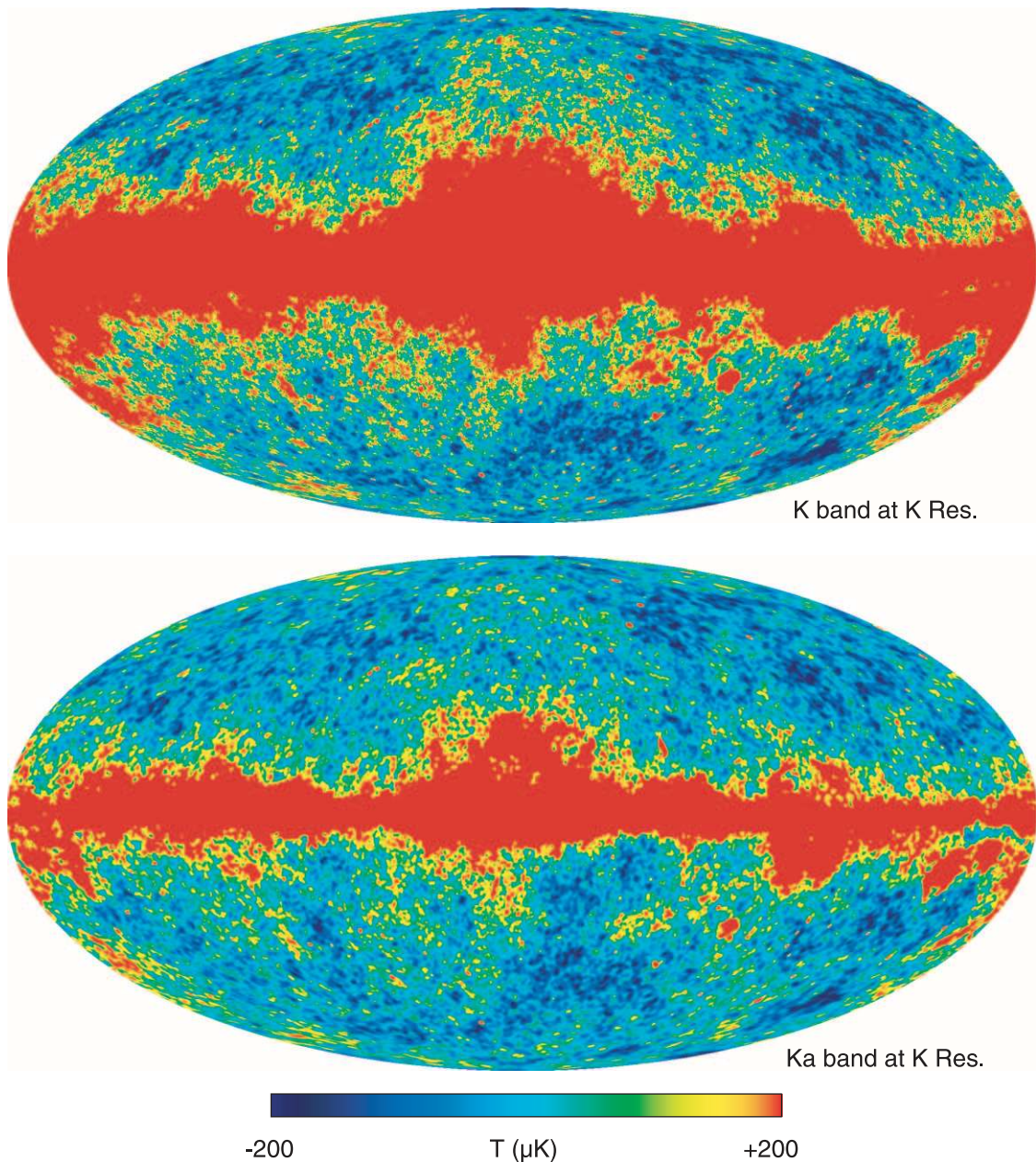


FIG. 5.—Comparison of the K-band map with the Ka-band map smoothed to K-band resolution, both in thermodynamic temperature, showing the dramatic reduction of Galactic contamination with increased frequency. The comparison also shows the similarity of the CMB fluctuation features at high Galactic latitude.

cannot be directly used in CMB analyses because of the complex noise properties that result from the MEM process and its simultaneous use of multifrequency maps. This is because the multifrequency maps are smoothed, different weights are used in different regions of the sky, and these weights are smoothed, all of which complicate the noise correlations. For the CMB analyses we use a mask to exclude pixels in which the Galactic emission is strong, combined with template fitting (using external data only) in which the foregrounds can be adequately corrected. This approach does not complicate the noise properties of the maps. The Kp2 cut is used for all analyses except for limits on non-Gaussianity and the temperature-polarization correlation function, in which the more severe Kp0 cut is used.

Bennett et al. (2003b) describe the template fitting in detail. Thermal dust emission has been mapped over the full sky in several infrared bands, most notably by the *COBE* and *IRAS* missions. A full-sky template is provided by Schlegel, Finkbeiner, & Davis (1998) and is extrapolated in frequency by Finkbeiner, Davis, & Schlegel (1999). The mostly synchrotron emission map of Haslam et al. (1981) at 408 MHz is used as a radio template. The free-free ionized gas is traced by the H α map assembled by Finkbeiner (2003) from the Wisconsin H-Alpha Mapper, the Virginia Tech Spectral-Line Survey, and the Southern H-Alpha Sky Survey Atlas (Dennison, Simonetti, & Topasna 1998; L. M. Haffner et al. 2003, in preparation; Reynolds, Haffner, & Madsen 2002; Gaustad et al. 2001). The Haslam map resolution is not as high as that of the *WMAP* maps, and the Haslam map has artifacts from

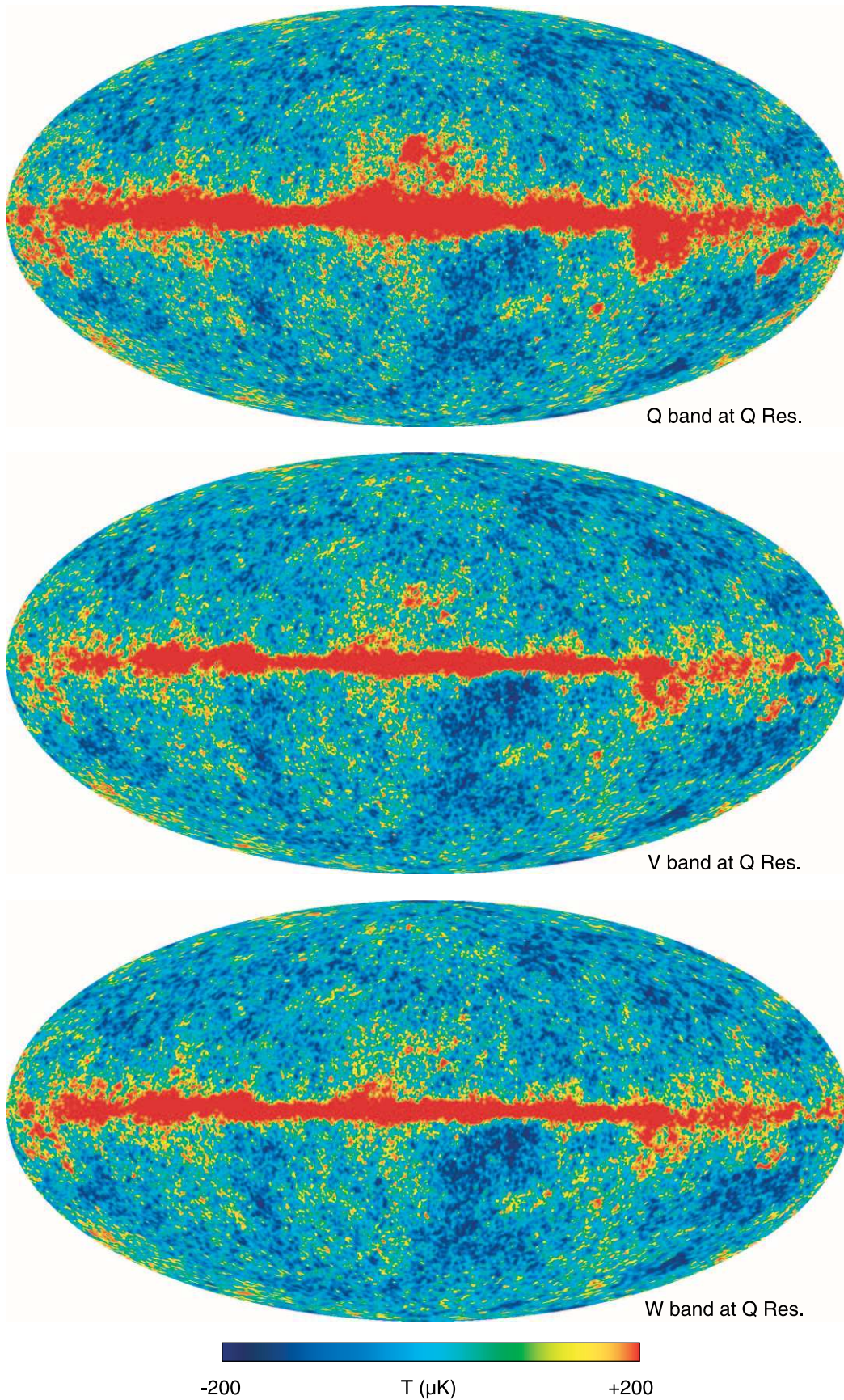


FIG. 6.—Comparison of the Q-band, V-band, and W-band maps. All three maps are smoothed to Q-band resolution and are in thermodynamic temperature. The reduction of Galactic contamination relative to the K band and Ka band (Fig. 5) is apparent. The maps show that the constant features across bands are CMB anisotropy, while the thermodynamic temperature of the foregrounds depends on the band (frequency).

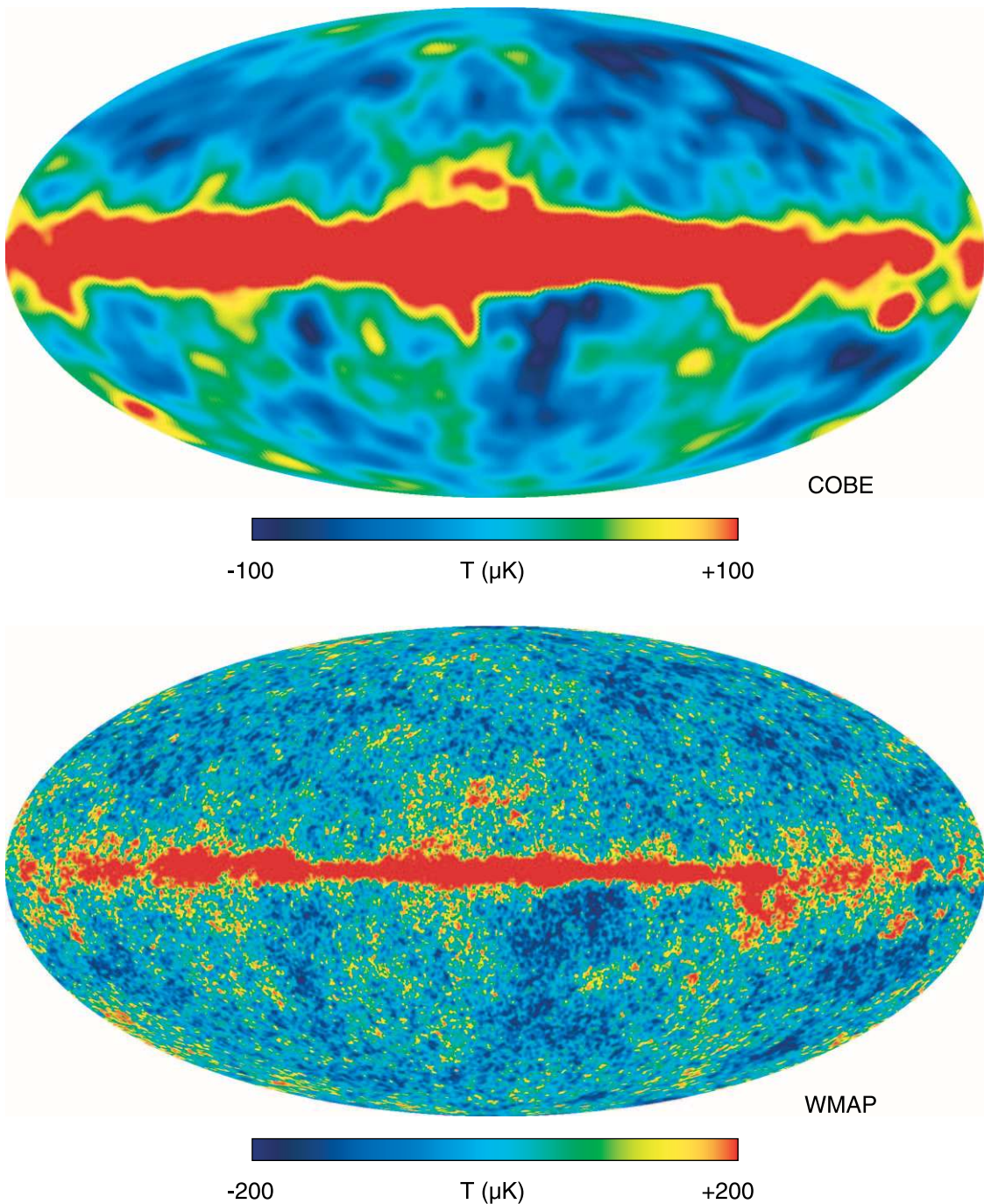


FIG. 7.—Comparison of the *COBE* 53 GHz map (Bennett et al. 1996) with the W-band *WMAP* map. The *WMAP* map has 30 times finer resolution than the *COBE* map.

experimental effects such as striping from spatial calibration variations. The striping in the Haslam map is along the survey scan lines and was corrected to first order by the application of a Wiener filter. (The filtered version of the Haslam map is publicly available on the Legacy Archive for Microwave Background Data Analysis [LAMBDA] Web site.) The remaining adverse effects of the Haslam map are mitigated by two effects: First, the template fit calls for only a small Haslam correlation (see § 6 of Bennett et al. 2003b). Since the correction is small, the error on the correction is negligible. Second, the foreground contamination is most significant

only on the largest angular scales, so the Haslam resolution limit and small-scale map artifacts are not significant sources of error. The MEM solution only uses the Haslam map as a prior, and the spinning dust limit only uses the full-sky median of the Haslam map. Thus, the spinning dust limit is insensitive to residual striping in the Haslam map.

The MEM results are used to assess the degree of foreground emission remaining after the template subtraction. The result is less than $7 \mu\text{K}$ rms at the Q band and less than $3 \mu\text{K}$ rms at both the V band and the W band for $\ell < 15$. This remaining foreground emission constitutes less than 2% of

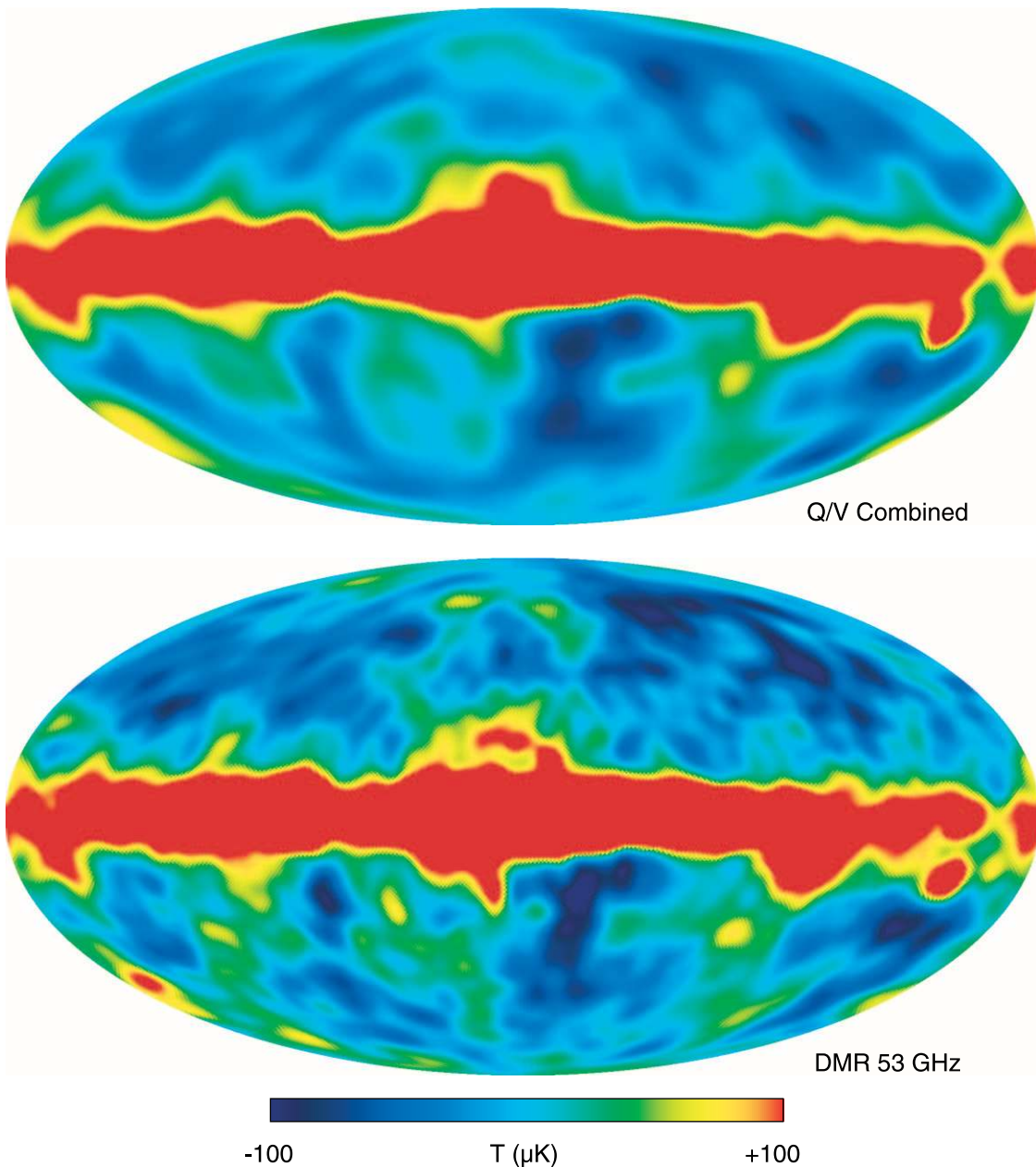


Fig. 8.—*COBE* DMR 53 GHz map (Bennett et al. 1996), shown along with a map made with a smoothed linear combination of the Q-band and V-band *WMAP* maps to mimic a 53 GHz map. Note the strong similarity of the maps.

the CMB variance (up to $\ell = 200$) in the Q band and $\lesssim 1\%$ of the CMB variance in the V and W bands. Figures 3 and 4 of Hinshaw et al. (2003b) demonstrate that this small residual foreground level has a negligible effect on the cosmological results.

5.3. Point Sources

A search was made for point sources in the *WMAP* data. A catalog of 208 detected sources (with 98% reliability) is provided by Bennett et al. (2003b). Statistically, five sources are expected to be false detections. Five of the 208 sources do not have low-frequency radio counterparts; these sources are likely to be the false detections. We include ~ 700 sources in our mask, despite having only detected ~ 200 sources at the 5σ level, because sources below this detection level still con-

tribute an undesirable statistical contamination to the maps. Even beyond masking the 700 sources, we still need to make a statistical correction to the power spectrum for residual source contamination (Hinshaw et al. 2003b). The derived source counts give a power spectrum level of $C^{\text{src}} = (15 \pm 3) \times 10^{-3} \mu\text{K}^2 \text{sr}$ at the Q band. This is consistent with the level found in the bispectrum analysis of the maps (Komatsu et al. 2003) and the level found in fits to the map power spectra (Hinshaw et al. 2003b). We have confidence that the point-source level is understood, since it is independently derived using three different methods.

5.4. Sunyaev-Zeldovich Effect

Hot gas in clusters of galaxies imparts energy to the CMB photons, causing a temperature decrement in the *WMAP*

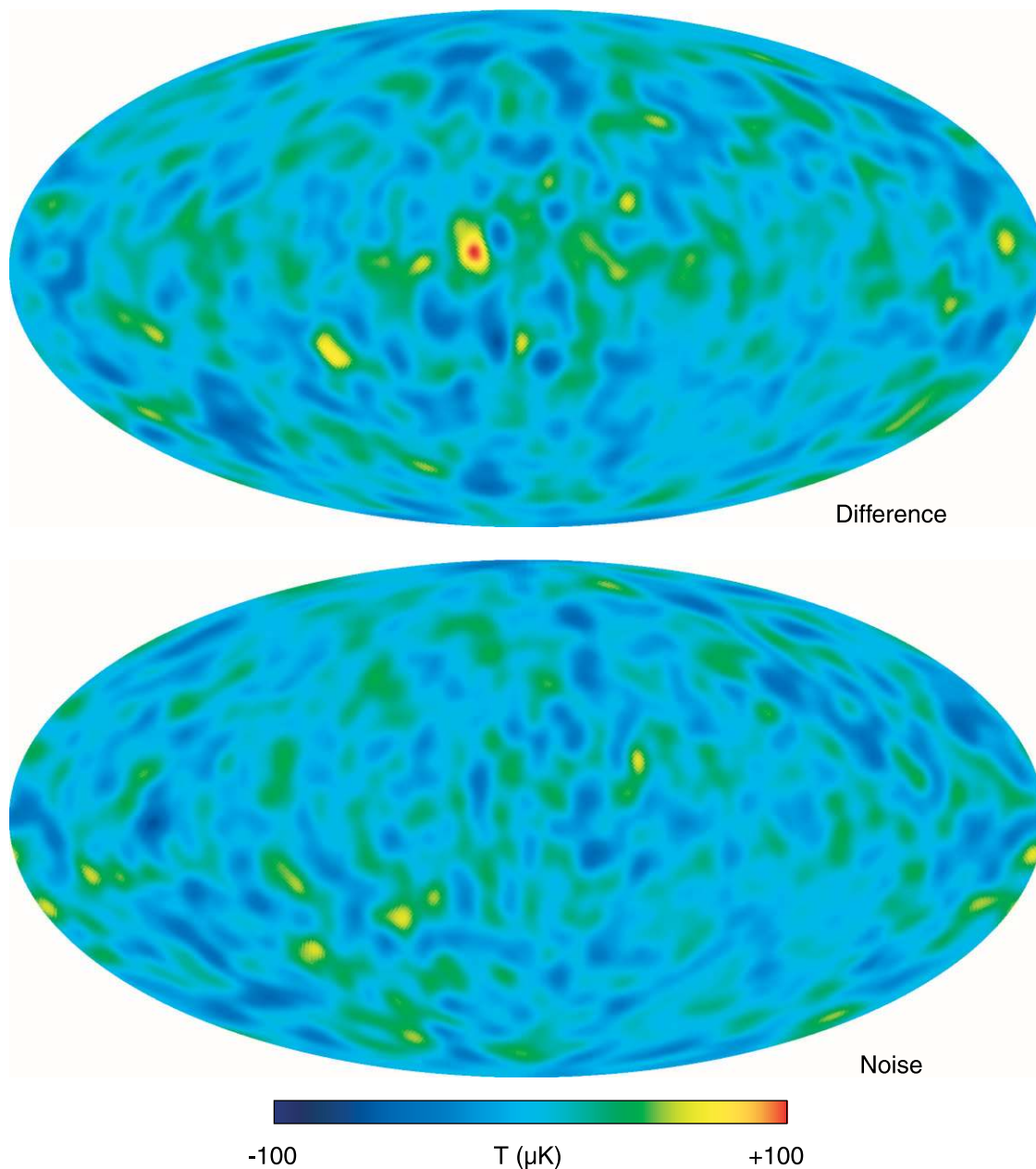


FIG. 9.—Difference map shown between the *COBE* DMR 53 GHz map and the combination Q-band/V-band maps from Fig. 8. This is compared with a map of the noise level. The maps are consistent with one another with the exception of a feature in the Galactic plane. This discrepancy is likely to be due to a spectral index that is sufficiently different from the assumed CMB spectrum used to combine the *WMAP* Q-band and V-band maps to mimic a 53 GHz map.

bands (the Sunyaev-Zeldovich effect). The Coma Cluster is expected to have the most pronounced signature. For the highest resolution maps, Bennett et al. (2003b) get -0.34 ± 0.18 mK in the W band and -0.24 ± 0.18 mK in the V band in the direction of Coma. Use of the XBACS catalog of X-ray clusters as a template results in -0.36 ± 0.14 . This verifies that the Sunyaev-Zeldovich effect is barely detectable in even a matched search of the *WMAP* sky maps, and therefore it is not a significant “contaminant” of the *WMAP* data.

6. LIMITS ON NON-GAUSSIANITY

Maps of the sky are the most complete and compact representation of the CMB anisotropy. Cosmological analyses

are based on statistical properties of the maps with the power spectrum as one of the most commonly derived statistics. The power spectrum is a complete representation of the data only if the CMB anisotropy is Gaussian. In addition, the most common cosmological models predict that the CMB anisotropy should be consistent with a Gaussian random field (at least at levels that are currently possible to measure). Therefore, we test the Gaussianity of the anisotropy, both to interpret the power spectrum (and other statistical derivatives of the maps) and to test cosmological paradigms.

There is no single best test for Gaussianity. Specific tests can be more or less sensitive to different assumed forms of non-Gaussianity. Komatsu et al. (2003), in a companion paper, search for non-Gaussianity in the *WMAP* CMB

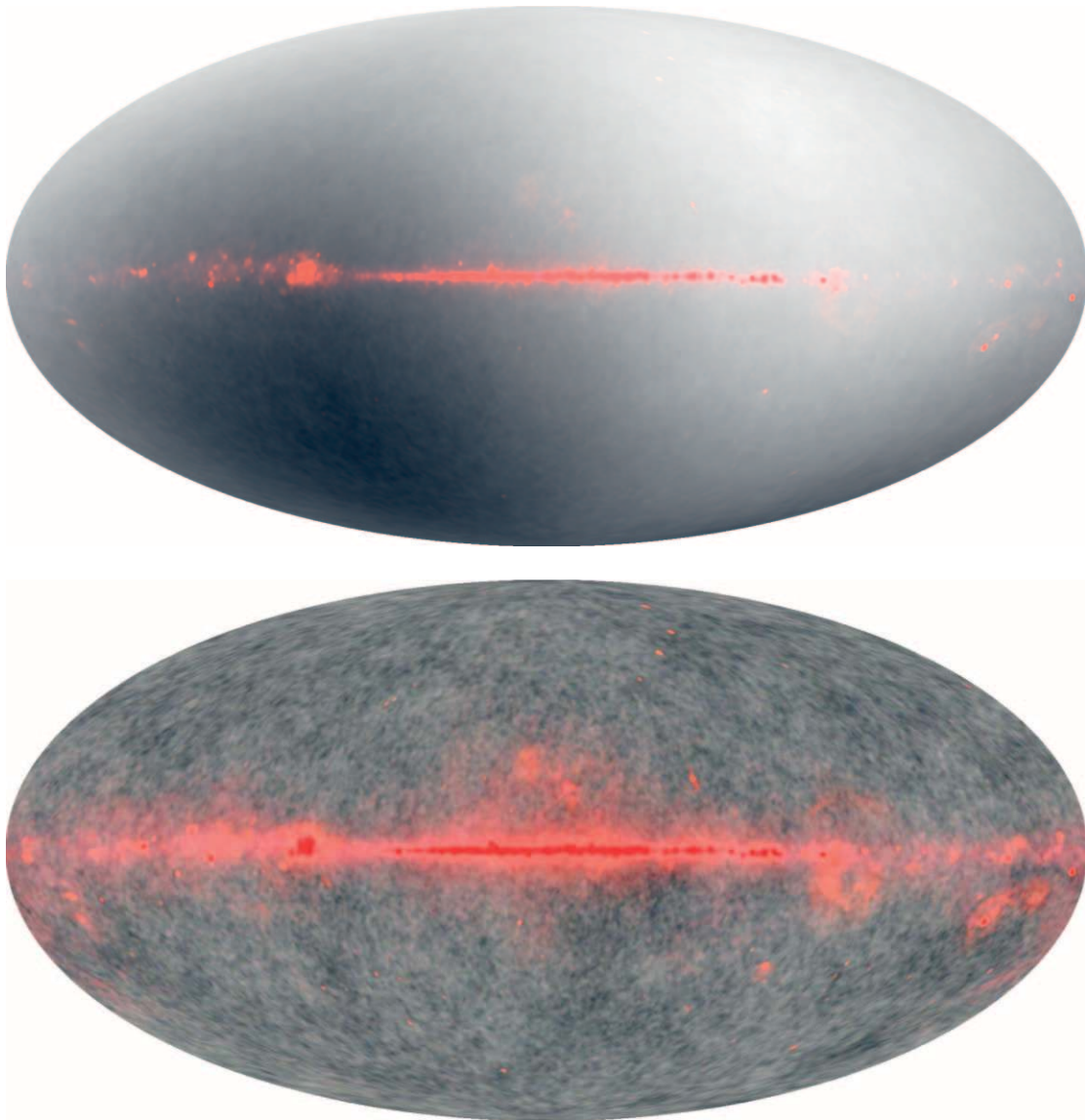


FIG. 10.—False-color images representing the spectral information from multiple *WMAP* bands. Q band is red, V band is green, and W band is blue. A CMB thermodynamic spectrum is gray. *Top*: Three-color combination image from the Q, V, and W-band maps. The dipole and high Galactic latitude anisotropy are seen. *Bottom*: Similar false-color image but with the dipole subtracted.

anisotropy maps using Minkowski functionals and a bispectrum estimator.

Minkowski functionals (Minkowski 1903; Gott et al. 1990) quantify topological aspects of the CMB maps. Anisotropy is examined via contours at different temperature levels, and the number and areas of regions enclosed by these contours are computed. Three Minkowski functionals are the area represented by hot and cold spots, the contour length around these areas, and the difference between the number of these areas (the “genus”).

It is widely believed that the CMB anisotropy arises from Gaussian linear fluctuations in the gravitational potential. Komatsu & Spergel (2001) suggest that non-Gaussian anisotropy be considered in terms of the curvature perturbation. The simplest expression for the overall primordial gravitational curvature perturbation, $\Phi(\mathbf{x})$, is a sum of a

linear $\Phi_L(\mathbf{x})$ and weak nonlinear components: $\Phi(\mathbf{x}) = \Phi_L(\mathbf{x}) + f_{\text{NL}}[\Phi_L^2(\mathbf{x}) - \langle \Phi_L(\mathbf{x}) \rangle^2]$, where Φ_L is the linear Gaussian portion of the curvature perturbation and f_{NL} is a nonlinear coupling constant. Then, $f_{\text{NL}} = 0$ corresponds to the purely linear Gaussian case. Since the CMB bispectrum measures the phase correlations of the anisotropy, it can be used to solve for f_{NL} . The Minkowski functional results can also be expressed in terms of f_{NL} .

For the Minkowski functionals, Komatsu et al. (2003) find $f_{\text{NL}} < 139$ (95% confidence level [CL]). From the bispectrum, Komatsu et al. (2003) find $-58 < f_{\text{NL}} < 134$ (95% CL). The two results are consistent. The CMB anisotropy is thus demonstrated to follow Gaussian statistics. This is a significant result for models of the early universe. It also means that we can construct and interpret CMB statistics (e.g., the angular power spectrum) from the maps in a straightforward manner.

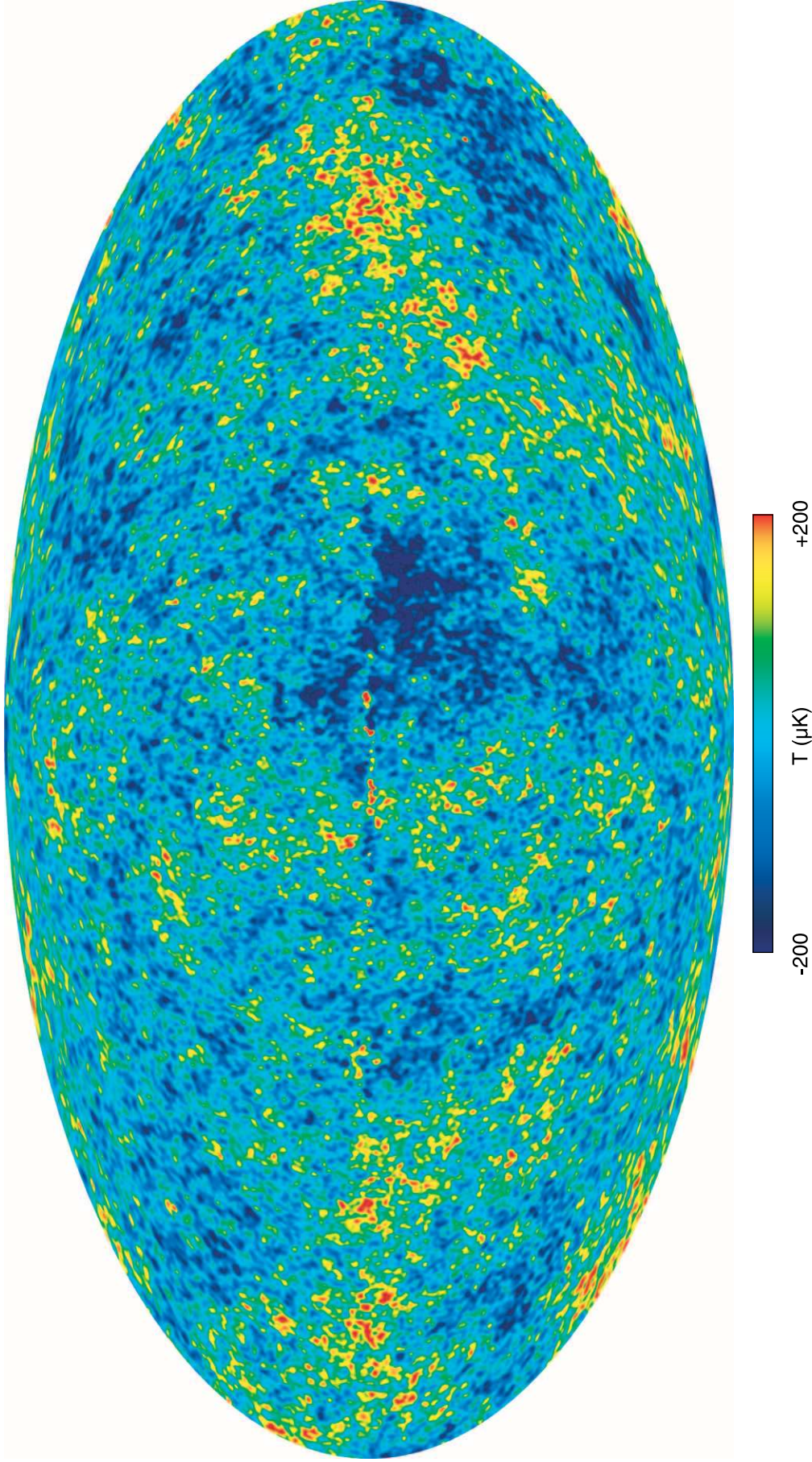


FIG. 11.—“Internal linear combination” map combining the five band maps in such a way as to maintain unity response to the CMB while minimizing foreground contamination. For a more detailed description, see Bennett et al. (2003b). For the region that covers the full sky outside of the inner Galactic plane, the weights are 0.109, -0.684 , -0.096 , 1.921, and -0.250 for the K, Ka, Q, V, and W bands, respectively. Note that there is a chance alignment of a particularly warm feature and a cool feature near the Galactic plane. As discussed in Bennett et al. (2003b), the noise properties of this map are complex, so it should not generally be used for cosmological analyses.

7. MULTIPOLES

The temperature anisotropy $T(\mathbf{n})$ is naturally expanded in a spherical harmonic basis $Y_{\ell m}$ as

$$T(\mathbf{n}) = \sum_{\ell, m} a_{\ell m} Y_{\ell m}(\mathbf{n}). \quad (1)$$

The angular power spectrum C_ℓ is a cosmological ensemble average given by

$$C_\ell = \langle |a_{\ell m}|^2 \rangle \quad (2)$$

and is observed for our actual sky as

$$C_\ell^{\text{sky}} = \frac{1}{2\ell + 1} \sum_m |a_{\ell m}|^2. \quad (3)$$

Assuming random phases, the temperature anisotropy for each multipole moment, ΔT_ℓ , can be associated with the angular spectrum C_ℓ as

$$\Delta T_\ell = \sqrt{\frac{C_\ell^{\text{sky}} \ell(\ell + 1)}{2\pi}} \quad (4)$$

The correlation function is

$$C(\theta) = \frac{1}{4\pi} \sum_\ell \sum_{m=-\ell}^{+\ell} C_\ell P_\ell(\cos \theta) \quad (5)$$

$$= \frac{1}{4\pi} \sum_\ell (2\ell + 1) C_\ell P_\ell(\cos \theta), \quad (6)$$

where P_ℓ is the Legendre polynomial of the order of ℓ .

In practice, an instrument adds noise and spatially filters the sky signal due to the beam pattern and any other experimental limitations on the sampling of all angular scales. The experimental transfer function b_ℓ for each multipole moment depends on the specific beam pattern of the experiment. *WMAP* samples all angular scales limited only by the beam pattern. The window function for the signal power between channels i and j is

$$w_\ell^{ij} = b_\ell^i b_\ell^j p_\ell^2, \quad (7)$$

where p_ℓ^2 is the pixel window function. The angular power spectrum then becomes

$$C_\ell = C_\ell^{ij} b_\ell^i b_\ell^j p_\ell^2 + N_\ell^i \delta_{ij}, \quad (8)$$

where N_ℓ^i is the power spectrum noise that results from the instrument noise, which is assumed to be uncorrelated between channels i and j .

Note that an autopower spectrum has twice the noise variance of a cross-power spectrum with the corresponding noise in each map. This follows from the property of Gaussian noise that

$$\langle (N_\ell^i)^2 (N_\ell^j)^2 \rangle = 2 \langle (N_\ell^i)^2 \rangle \langle (N_\ell^j)^2 \rangle + \langle (N_\ell^i)^2 \rangle \langle (N_\ell^j)^2 \rangle,$$

with

$$\langle N_\ell^i N_\ell^j \rangle^2 = \langle (N_\ell^i)^2 \rangle \langle (N_\ell^j)^2 \rangle \quad \text{and} \quad \langle (N_\ell^i)^4 \rangle = 3 \langle (N_\ell^i)^2 \rangle^2.$$

The use of a sky mask for foreground suppression breaks the orthogonality of the spherical harmonics on the sky and leads to mode coupling. Hinshaw et al. (2003b) discuss how *WMAP* handles this, and other complexities.

7.1. $\ell = 1$ Dipole

COBE determined the dipole amplitude is 3.353 ± 0.024 mK in the direction

$$(l, b) = (264^\circ 26 \pm 0^\circ 33, 48^\circ 22 \pm 0^\circ 13),$$

where l is Galactic longitude and b is Galactic latitude (Bennett et al. 1996). This dipole was subtracted from the *WMAP* data during processing. Examination of a residual dipole, and thus an improvement over the *COBE* value. Note that this does not have any effect on *WMAP* calibration, which is based on the Earth's velocity modulation of the dipole and not on the dipole itself. The *WMAP*-determined dipole is 3.346 ± 0.017 mK in the direction $(l, b) = (263^\circ 85 \pm 0^\circ 1, 48^\circ 25 \pm 0^\circ 04)$. The uncertainty of the dipole amplitude is limited by the *WMAP* 0.5% calibration uncertainty, which will improve with time.

7.2. $\ell = 2$ Quadrupole

The quadrupole is the $\ell = 2$ term of the spectrum $\Delta T_\ell^2 = \ell(\ell + 1) C_\ell / 2\pi$, i.e., $\Delta T_{\ell=2}^2 = (3/\pi) C_{\ell=2}$. Alternately, the quadrupole amplitude can be expressed as $Q_{\text{rms}} = [(5/4\pi) C_{\ell=2}]^{1/2} = (5/12)^{1/2} \Delta T_{\ell=2}$. The 4 year *COBE* quadrupole is $Q_{\text{rms}} = 10_{-4}^{+7} \mu\text{K}$, with the peak of the likelihood in the range $6.9 \mu\text{K} < Q_{\text{rms}} < 10 \mu\text{K}$, as shown in Figure 1 of Hinshaw et al. (1996b).

The *WMAP* quadrupole, $Q_{\text{rms}} = 8 \pm 2 \mu\text{K}$ or $\Delta T_2^2 = 154 \pm 70 \mu\text{K}^2$, is consistent with *COBE* but with tighter limits because of better measurements and understanding of foregrounds. We determine the quadrupole value by computing the power spectrum of the internal linear combination map and individual channel maps, with and without foreground corrections, for a range of Galactic cuts. The final $\ell = 2$ value corresponds to a full-sky estimate with an uncertainty that encompasses a range of foreground-masked or foreground-corrected solutions. The foreground level is still the leading uncertainty. (The small kinematic quadrupole is neither removed from the maps nor accounted for in this analysis.) The quadrupole value is low compared to values predicted by Λ -dominated cold dark matter (ΛCDM) models that fit the rest of the power spectrum. ΛCDM models, in particular, tend to predict relatively high quadrupole values due to the enhanced, Λ -driven, integrated Sachs-Wolfe effect.

7.3. n -Poles

A central part of the task of computing multipole information from the maps is the evaluation and propagation of errors and uncertainties. This largely involves arriving at an adequate representation of the Fisher matrix, which is the inverse covariance matrix of the data. The Fisher matrix must take into account mode coupling from the sky cut, beam (window function) uncertainties, and noise properties. The fact that the *WMAP* data use a nearly azimuthally symmetric cut and have a nearly diagonal pixel-pixel covariance greatly simplifies the evaluation of the Fisher matrix.

Two approaches to computing the angular power spectrum have been used by Hinshaw et al. (2003b): a quadratic estimation based on Hivon et al. (2002) and a maximum likelihood estimate based on Oh, Spergel, & Hinshaw (1999). The quadratic estimator is used in the final *WMAP*

spectrum analyses, while the maximum likelihood technique is used as a cross-check.

The K-band and Ka-band beam sizes are large enough that these bands are not used for CMB analysis, since they have the most foreground contamination and probe the region in ℓ -space that is cosmic-variance-limited by the measurements at the other bands. These bands are invaluable, however, as monitors of Galactic emission. The two Q-band, two V-band, and four W-band differencing assemblies are the source of the prime CMB data. The matrix of auto- and cross-correlations between the eight Q, V, and W-band differencing assemblies has eight diagonal (auto-correlations) and 28 unique off-diagonal elements (cross-correlations). Since autocorrelations are difficult to assess because of the noise bias (see eq. [8]), we included only the 28 unique cross-correlations in the *WMAP* power spectrum analysis. In dropping the autocorrelations, each of which has twice the noise variance of a cross-correlation, we lose only $1 - [56/(56 + 8)]^{1/2} = 6\%$ of the ideally achievable signal-to-noise ratio. In Hinshaw et al. (2003b), we show that the power spectrum computed from the autocorrelation data is consistent with the angular power spectrum from the cross-correlation data. We anticipate using the autocorrelation data in future analyses.

The cross-power spectrum from the 28 pairs is considered in four ℓ -ranges. For $\ell \leq 100$ we use uniform pixel weighting of only V- and W-band data. This reduces the Galactic contamination where measurement errors are well below the cosmic variance. For $100 < \ell \leq 200$ we use uniform pixel weighting of the combined 28 pairs. For $200 < \ell \leq 450$ all 28 cross-power pairs are used with a transitional pixel weighting. The transitional pixel weighting, defined and discussed in detail in Appendix A of Hinshaw et al. (2003b), smoothly transitions the weighting from the uniform pixel weights in the signal-dominated $\ell < 200$ multipole regime to inverse noise variance weighting in the noise-dominated $\ell > 450$ multipole regime. For $\ell > 450$ all 28 pairs are used with inverse noise weighting. Our Monte Carlo simulations show that this approach is a nearly optimal scheme.

The angular power spectrum is shown for the *WMAP* data in Figure 12. The *WMAP* power spectrum agrees closely with *COBE* at the largest angular scales, and with the Cosmic Background Imager (CBI) and the Arcminute Cosmology Bolometer Array Receiver (ACBAR) at the finer angular scales. We highlight the CBI and ACBAR results because they are a useful complement to *WMAP* at the smaller angular scales. The acoustic pattern is obvious. Page et al. (2003c) find that the first acoustic peak is $\Delta T_\ell = 74.7 \pm 0.5 \mu\text{K}$ at $\ell = 220.1 \pm 0.8$. The trough following this peak is $41.0 \pm 0.5 \mu\text{K}$ at $\ell = 411.7 \pm 3.5$, and the second peak is $48.8 \pm 0.9 \mu\text{K}$ at $\ell = 546 \pm 10$.

Λ CDM models predict enhanced large-angle power due to the integrated Sachs-Wolfe effect. The *WMAP* and *COBE* data, on the other hand, have the opposite trend. The conflict is also seen clearly in the correlation function $C(\theta)$ shown in Figure 13. The *WMAP* correlation function is computed using the Kp0 cut on a combination of the Q-band, V-band, and W-band maps with the MEM Galactic model removed. The *COBE* correlation function is computed on the ‘‘custom cut’’ sky (Bennett et al. 1996). The best-fit Λ CDM model is shown with a gray band indicating 1σ as determined by Monte Carlo simulations.

The lower two plots in Figure 13 display the correlation function of the difference between the *COBE* DMR and

WMAP maps with a $|b| = 10^\circ$ Galactic plane cut. A synthesis of the *WMAP* Q- and V-band maps was made to approximate a 53 GHz map to compare with the *COBE* DMR 53 GHz map. The *COBE* DMR 90 GHz map is compared directly, without corrections, to the *WMAP* W-band map. These plots emphasize the consistency of the *WMAP* and *COBE* measurements. The slightly higher than expected deviations at 53 GHz are likely to be due to Galactic contamination, arising from outside the cut regions and from the construction of the synthesized *WMAP* 53 GHz map.

The model is an excellent fit to the *WMAP* full power spectrum except, perhaps, at $\ell \lesssim 6$. Since only a small fraction of the total number of measured multipoles are involved, the statistical contribution of the $\ell \lesssim 6$ points to the overall power spectrum fit is small and does not greatly drive the overall best-fit model. The correlation function emphasizes the low- ℓ signal because these modes contribute to $C(\theta)$ at all angular separations. The discrepancy at $\theta \lesssim 30^\circ$ reflects the average lack of power in the data relative to the model at $\ell < 6$. More significantly, the lack of power at $\theta \gtrsim 60^\circ$ relative to the model reflects the special shape of the power spectrum from $2 < \ell < 5$ seen in both the *WMAP* and *COBE* maps. This result is generically true for Λ CDM models, independent of the exact parameters of the model. *There is very little large-scale CMB anisotropy power in our sky. This fact, first seen by COBE, is confirmed by WMAP.* The probability of so little $C(\theta > 60^\circ)$ anisotropy power is $\sim 2 \times 10^{-3}$, given the best-fit Λ CDM model. The lack of power is seen in both $C(\theta)$ and the behavior of the low-order ($\ell = 2, 3, 4$, and 5) multipoles.

8. CMB POLARIZATION AND THE DETECTION OF REIONIZATION

Each differencing assembly measures the sky in two orthogonal linear polarizations. As the observatory spins, precesses, and orbits the Sun, the instrument observes the sky over a range of polarization angles. The range of angles observed is neither complete nor uniform, but it is sufficient to provide valuable new CMB polarization results.

We express polarization in terms of the standard I , Q , and U Stokes parameters, in units of thermodynamic temperature. Polarization coordinates are not rotationally invariant, so a coordinate system is defined by Kogut et al. (2003) for expressing information. By appropriate summing and differencing of the TOD from the pairs of corresponding radiometers, we iteratively make maps in unpolarized intensity I and in each polarized component, Q and U (Hinshaw et al. 2003b). The Q and U maps not only have a much lower signal-to-noise ratio than the I maps, but they are more susceptible to systematic errors, since the differencing between radiometer outputs occurs on the ground, not in the front end of the radiometers.

The U polarization maps are expected to be the most affected by systematic errors. This is due to the orientation of the observed polarization angles relative to the spin axis of the observatory, causing systematics not fixed on the sky to preferentially go into the U map.

Taurus A, an extremely strong source in the *WMAP* bands, is polarized, and its polarization amplitude and direction are known (Flett & Henderson 1979). Polarization measurements from *WMAP* are consistent with previous observations of Taurus A, providing a useful check on the operation of the *WMAP* hardware and software. However,

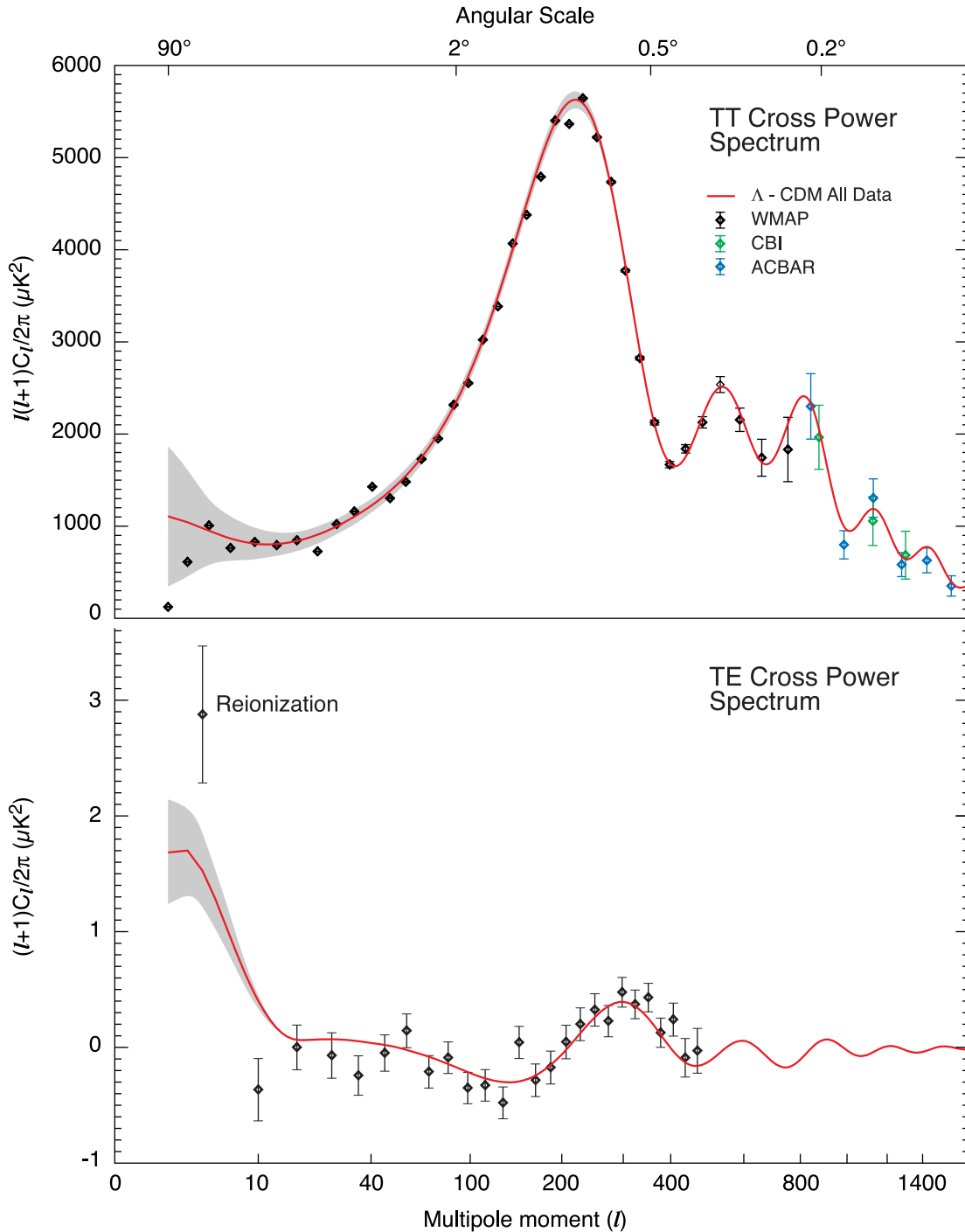


FIG. 12.—*WMAP* angular power spectrum. *Top*: *WMAP* temperature (TT) results, consistent with the ACBAR and CBI measurements, as shown. The TT angular power spectrum is now highly constrained. Our best-fit running index Λ CDM model is shown. The gray band represents the cosmic variance expected for that model. The quadrupole has a surprisingly low amplitude. In addition, there are excursions from a smooth spectrum (e.g., at $l \approx 40$ and 210) that are only slightly larger than expected statistically. While intriguing, they may result from a combination of cosmic variance, subdominant astrophysical processes, and small effects from approximations made for this first-year data analysis (Hinshaw et al. 2003b). We do not attach cosmological significance to them at present. More integration time and more detailed analyses are needed. *Bottom*: TE cross-power spectrum, $(l+1)C_l/2\pi$. (Note that this is *not* multiplied by the additional factor of l .) The peak in the TE spectrum near $l \sim 300$ is out of phase with the TT power spectrum, as predicted for adiabatic initial conditions. The antipeak in the TE spectrum near $l \sim 150$ is evidence for superhorizon modes at decoupling, as predicted by inflationary models.

the polarization systematic errors have not yet been fully quantified. We chose to release the I data and results as soon as possible, rather than postpone their publication and release until the systematic measurement errors of the Q and U data are fully assessed. All data, including the Q and U

maps, will be released when the characterization of their instrumental signatures is complete. The dominant systematic effect in the low signal-to-noise ratio polarization data arises from correlated noise in the radiometers. By using only cross-correlations of temperature maps with polariza-

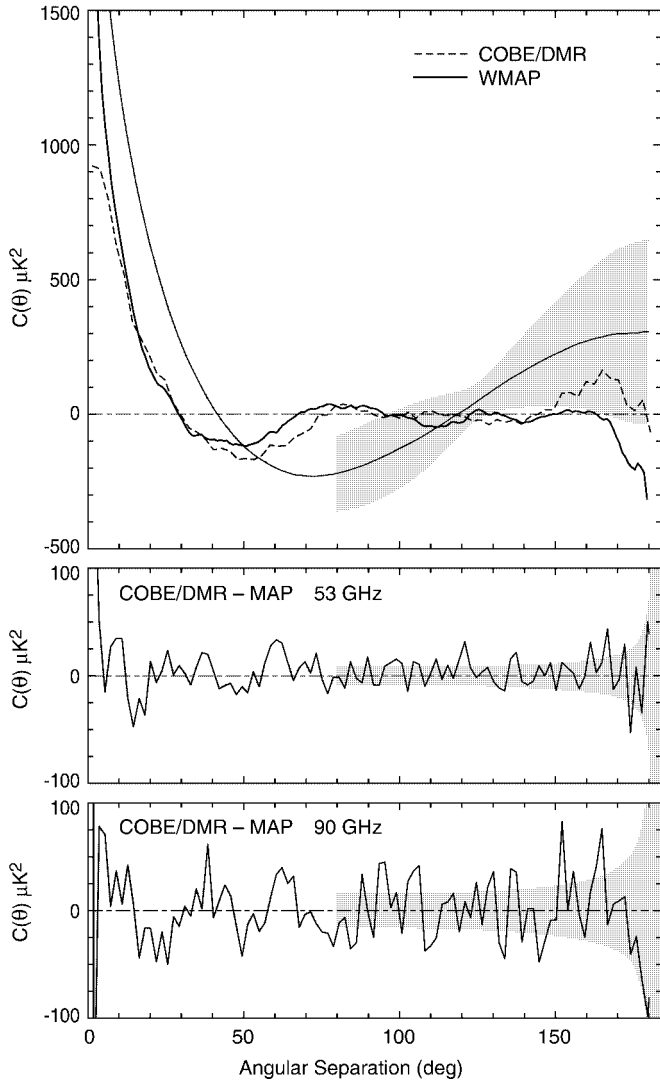


FIG. 13.—*Top*: CMB temperature correlation function of the *WMAP* and *COBE* data. The *WMAP* correlation function is computed using a combination of the Q-band, V-band, and W-band maps with the Kp0 cut sky and the MEM Galactic model subtracted. The *COBE* correlation function is computed using the “custom cut” sky. The running index Λ CDM model that is fitted to the power spectrum is shown with a Monte Carlo-determined gray band indicating 1σ . The model is, overall, an excellent fit to the *WMAP* power spectrum. However, a correlation plot emphasizes the low- ℓ power. The discrepancy between the model and data illustrates that there is surprisingly little anisotropy power in the *WMAP* and *COBE* maps at large angles. *Bottom*: The lower two plots display the correlation function of the difference between the *COBE* DMR and *WMAP* maps with a $|b| = 10^\circ$ Galactic plane cut. A synthesis of the *WMAP* Q- and V-band maps was made to approximate a 53 GHz-like map to compare with the *COBE* DMR 53 GHz map. The *COBE* DMR 90 GHz map is compared directly, without corrections, to the *WMAP* W-band map. These plots emphasize the consistency of the *WMAP* and *COBE* measurements. The slightly higher than expected deviations at 53 GHz are likely to be due to Galactic contamination, arising from outside the cut regions and from the construction of the synthesized *WMAP* 53 GHz map.

tion maps, generated from independent radiometer combinations that have uncorrelated noise, we mitigate the leading systematic error. For this reason, results of temperature-polarization correlations between the I and Q maps, i.e., temperature-polarization (TE) correlations, are much less sensitive to systematic effects than polarization signals alone, so we are able to report those results.

Figure 12 shows the TE cross-power spectrum. Kogut et al. (2003) report a detection of TE correlations on both large angular scales (from reionization) and small scales (from the adiabatic fluctuations). The TE power spectrum, shown in Figure 12, is discussed in detail by Kogut et al. (2003). In the TE angular power spectrum, the antipeak is $-35 \pm 9 \mu\text{K}^2$ at $\ell = 137 \pm 9$, and the peak is $105 \pm 18 \mu\text{K}^2$ at $\ell = 329 \pm 19$ (Page et al. 2003c).

The detection of the reionization of the universe corresponds to an optical depth $\tau = 0.17 \pm 0.04$ ($0.09 \leq \tau \leq 0.28$ at 95% CL). Although *WMAP* measures the integrated optical depth, the epoch and redshift of reionization can be derived from the integral optical depth within the context of a model of the reionization process. A single instantaneous step function in the ionization fraction from zero to a steady fixed value is physically unlikely. For more likely models, Kogut et al. (2003) conclude that the redshift of reionization is $z_r = 20_{-9}^{+10}$ (95% CL), corresponding to an epoch of reionization of $t_r = 180_{-80}^{+220}$ Myr (95% CL) after the big bang. Cen (2003) presents a detailed model of a reionization process and predicts an integral value of the optical depth, $\tau = 0.10 \pm 0.03$. This is low compared to the newly measured value but would be higher and consistent if the assumed cosmological parameters in the model were adjusted to the values of the new *WMAP* best-fit parameters (see § 9.1).

The measured optical depth means that reionization suppressed the acoustic peak amplitudes by $1 - e^{-2\tau} \approx 30\%$. While accounted for in our model fits (§ 9), this suppression was not accounted for in previous CMB parameter determinations. The anticorrelations observed in the TE power spectrum directly imply superhorizon fluctuations, a new result in support of inflation-like theories, as discussed in § 9.3.

9. COSMOLOGICAL INTERPRETATION

In this section we summarize the cosmological interpretation of *WMAP* first-year results, which are discussed in more detail by Spergel et al. (2003), Peiris et al. (2003), Page et al. (2003c), and Kogut et al. (2003). The methodology used in the model fits is described by Verde et al. (2003).

Spergel et al. (2003) show that a cosmological model with a flat universe, seeded with a scale-invariant spectrum of adiabatic Gaussian fluctuations, and with reionization is an acceptable fit not only to the *WMAP* data but also to a host of astronomical data. These data are smaller angular scale CMB anisotropy data from ACBAR (Kuo et al. 2002) and CBI (Pearson et al. 2003), the *Hubble Space Telescope* (*HST*) Key Project value of H_0 (Freedman et al. 2001), the accelerating universe seen in Type Ia supernovae (Riess et al. 2001), the shape and amplitude of the large-scale structure seen in clusters and superclusters of galaxies (Percival et al. 2001; Verde et al. 2003), and the linear matter power spectrum seen in the $\text{Ly}\alpha$ forest (Croft et al. 2002). There has been mounting evidence in the direction of this model for years (Peebles 1984; Bahcall et al. 1999). The optical depth since reionization is a new, but not surprising, component of the model. The *WMAP* data establish this model as the standard model of cosmology by testing the key assumptions of the model and by enabling a precise determination of its parameters.

The *WMAP* data test several of the key tenets of the standard model. The *WMAP* detection of temperature-

polarization correlations (Kogut et al. 2003) and the clear detection of acoustic peaks (Page et al. 2003c) imply that the primordial fluctuations were primarily adiabatic: the primordial ratio of dark matter/photons and the primordial ratio of baryons/photons do not vary spatially. The analysis of the *WMAP* temperature data demonstrates Gaussianity (Komatsu et al. 2003). The *WMAP* data, when combined with any one of the following three external data sets, the *HST* Key Project measurement of H_0 (Freedman et al. 2001), the Two-Degree Field Galaxy Redshift Survey (2dFGRS) measurement of the matter density (Percival et al. 2001; Verde et al. 2003), or the Type Ia supernova measurements (Riess et al. 2001), imply that the radius of curvature of the universe, $R = cH_0^{-1}|1 - \Omega_{\text{tot}}|^{-1/2}$, must be very large: $\Omega_{\text{tot}} = 1.02 \pm 0.02$ and $0.99 < \Omega_{\text{tot}} < 1.05$ (95% CL). These measurements also require that the dark energy be the dominant constituent of Ω_{tot} . The *WMAP* data alone rule out the standard $\Omega_m = 1$ CDM model by more than 7σ .

9.1. Best-Fit Cosmological Model

While an acceptable fit, the model described above is not our best-fit model. In the discussion below we concentrate

on our best-fit model, which adds a scale-dependent primordial spectral index. This cosmological model is a flat universe with a baryon fraction of $\Omega_b = 0.044 \pm 0.004$, a matter fraction of $\Omega_m = 0.27 \pm 0.04$, and a dark energy fraction of $\Omega_\Lambda = 0.73 \pm 0.04$, seeded with a scale-dependent spectrum of adiabatic Gaussian fluctuations. This model has $C_{\ell=10} = 46.0 \mu\text{K}^2$, consistent with the *COBE* measurement of $C_{\ell=10} = 44.4 \mu\text{K}^2$.

The *WMAP* data alone enable accurate determinations of many of the key cosmological parameters (Spergel et al. 2003). However, a combination of the *WMAP* data with the *COBE* determination of the CMB temperature (Mather et al. 1999), the CBI (Pearson et al. 2003) and the ACBAR (Kuo et al. 2002) CMB measurements, and the 2dFGRS survey determination of the power spectrum of the local galaxy fluctuations (Percival et al. 2001) yields the best-fit cosmological parameters, listed in Table 3. Verde et al. (2003) describe our methodology for determining these parameters, and Spergel et al. (2003) describe the best-fit models for different combinations of data sets.

A power spectrum of primordial mass fluctuations with a scale-invariant spectral index is given by $P(k) = Ak^{n_s}$ with $n_s = d \ln P/d \ln k$. Inflationary models predict a running spectral index (Kosowsky & Turner 1995), and our best-fit

TABLE 3
“BEST” COSMOLOGICAL PARAMETERS

Description	Symbol	Value	+ Uncertainty	– Uncertainty
Total density	Ω_{tot}	1.02	0.02	0.02
Equation of state of quintessence	w	< -0.78	95% CL	...
Dark energy density	Ω_Λ	0.73	0.04	0.04
Baryon density	$\Omega_b h^2$	0.0224	0.0009	0.0009
Baryon density	Ω_b	0.044	0.004	0.004
Baryon density (cm^{-3})	n_b	2.5×10^{-7}	0.1×10^{-7}	0.1×10^{-7}
Matter density	$\Omega_m h^2$	0.135	0.008	0.009
Matter density	Ω_m	0.27	0.04	0.04
Light neutrino density	$\Omega_\nu h^2$	< 0.0076	95% CL	...
CMB temperature (K) ^a	T_{CMB}	2.725	0.002	0.002
CMB photon density (cm^{-3}) ^b	n_γ	410.4	0.9	0.9
Baryon-to-photon ratio	η	6.1×10^{-10}	0.3×10^{-10}	0.2×10^{-10}
Baryon-to-matter ratio	$\Omega_b \Omega_m^{-1}$	0.17	0.01	0.01
Fluctuation amplitude in $8 h^{-1}$ Mpc spheres	σ_8	0.84	0.04	0.04
Low- z cluster abundance scaling	$\sigma_8 \Omega_m^{0.5}$	0.44	0.04	0.05
Power spectrum normalization (at $k_0 = 0.05 \text{ Mpc}^{-1}$) ^c	A	0.833	0.086	0.083
Scalar spectral index (at $k_0 = 0.05 \text{ Mpc}^{-1}$) ^c	n_s	0.93	0.03	0.03
Running index slope (at $k_0 = 0.05 \text{ Mpc}^{-1}$) ^c	$dn_s/d \ln k$	-0.031	0.016	0.018
Tensor-to-scalar ratio (at $k_0 = 0.002 \text{ Mpc}^{-1}$)	r	< 0.90	95% CL	...
Redshift of decoupling	z_{dec}	1089	1	1
Thickness of decoupling (FWHM)	Δz_{dec}	195	2	2
Hubble constant	h	0.71	0.04	0.03
Age of universe (Gyr)	t_0	13.7	0.2	0.2
Age at decoupling (kyr)	t_{dec}	379	8	7
Age at reionization (Myr, 95% CL)	t_r	180	220	80
Decoupling time interval (kyr)	Δt_{dec}	118	3	2
Redshift of matter-energy equality	z_{eq}	3233	194	210
Reionization optical depth	τ	0.17	0.04	0.04
Redshift of reionization (95% CL)	z_r	20	10	9
Sound horizon at decoupling (deg)	θ_A	0.598	0.002	0.002
Angular size distance (Gpc)	d_A	14.0	0.2	0.3
Acoustic scale ^d	ℓ_A	301	1	1
Sound horizon at decoupling (Mpc) ^d	r_s	147	2	2

^a From *COBE* (Mather et al. 1999).

^b Derived from *COBE* (Mather et al. 1999).

^c With $\ell_{\text{eff}} \approx 700$.

^d With $\ell_A \equiv \pi \theta_A^{-1}$, $\theta_A \equiv r_s d_A^{-1}$.

model uses a power spectrum of primordial mass fluctuations with a scale-dependent spectral index:

$$P(k) = P(k_0) \left(\frac{k}{k_0} \right)^{n_s(k_0) + (1/2)(dn_s/d \ln k) \ln(k/k_0)} \quad (9)$$

As in the scale-independent case, we define

$$n_s(k) \equiv \frac{d \ln P}{d \ln k}, \quad (10)$$

so

$$n_s(k) = n_s(k_0) + \frac{dn_s}{d \ln k} \ln \left(\frac{k}{k_0} \right) \quad (11)$$

(with $d^2 n_s / d \ln k^2 = 0$). The definition for n_s used here includes a factor of $\frac{1}{2}$ difference from the Kosowsky & Turner (1995) definition. Peiris et al. (2003) explore the implications of this running spectral index for inflation. The best-fit values of A , n_s , and $dn_s/d \ln k$ are in Table 3 for $k_0 = 0.05 \text{ Mpc}^{-1}$. The quantity A is the normalization parameter in CMBFAST, version 4.1, with option UNNORM. The amplitude of curvature fluctuations at the horizon crossing is $|\Delta_R(k_0)|^2 = 2.95 \times 10^{-9} A$. We discuss the implications of the measured values of these parameters in § 9.3 and in Peiris et al. (2003).

The *WMAP* data constrain the properties of both the dark matter and the dark energy in the following ways:

1. The *WMAP* detection of reionization at $z \sim 20$ is incompatible with the presence of significant warm dark matter density. Since the warm dark matter moves too fast to cluster in small objects, the first objects do not form in this scenario until $z \sim 8$ (Barkana, Haiman, & Ostriker 2001).

2. The running spectral index implies a lower amplitude for mass fluctuations on the dwarf galaxy scale. Dark matter simulations of models (Ricotti 2002) find that the dark matter mass profiles depend on the spectral index on the relevant mass scale. Thus, the shallower spectral index implied by our best-fit model may solve the CDM dark matter halo profile problem (Moore et al. 1998; Spergel & Steinhardt 2000).

3. While the *WMAP* data alone are compatible with a wide range of possible properties for the dark energy, the combination of the *WMAP* data with either the *HST* Key Project measurement of H_0 , the 2dFGRS measurements of the galaxy power spectrum, or the Type Ia supernova measurements requires that the dark energy be 73% of the total density of the universe and that the equation of state of the dark energy satisfy $w < -0.78$ (95% CL).

9.2. Best-Fit Parameters

WMAP's measurements of the baryon density, Hubble constant, and age of the universe strengthen the cosmic consistency that underlies the big bang model.

Atomic density ($\Omega_b h^2$).—*WMAP* measures the atomic density at recombination to an accuracy of 4% through the shape of the angular power spectrum, and particularly through the ratio of the heights of the first to second peak (Page et al. 2003c; Spergel et al. 2003). Our best-fit value is $\Omega_b h^2 = 0.0224 \pm 0.0009$. The baryon density is also probed via abundance measurements of [D]/[H] (O'Meara et al.

2001; Pettini & Bowen 2001; D'Odorico, Dessauges-Zavadsky, & Molaro 2001). It is impressive that $\Omega_b h^2$ is the same at $z = 1089$ as measured via the CMB as it is at $z = 10^9$ from big bang nucleosynthesis. Thus, we find cosmic consistency of the baryon density throughout cosmic time and measurement technique.

Hubble constant (H_0).—The *WMAP* measurements of the age and $\Omega_m h^2$ yield a measurement of $H_0 = 71_{-3}^{+4} \text{ km s}^{-1} \text{ Mpc}^{-1}$ that is remarkably consistent with the *HST* Key Project value of $H_0 = 72 \pm 3 \pm 7 \text{ km s}^{-1} \text{ Mpc}^{-1}$ (Freedman et al. 2001), but with smaller uncertainty. Recent measurements of the Hubble constant from gravitational lens timing and the Sunyaev-Zeldovich effect yield independent estimates that are generally consistent but with larger uncertainties at present. Through a variety of measurement techniques that sample different cosmic times and distances, we find cosmic consistency on H_0 .

Age of the universe (t_0).—The first acoustic peak in the CMB power spectrum represents a known acoustic size ($r_s = 147 \pm 2 \text{ Mpc}$) at a known redshift ($z_{\text{dec}} = 1089 \pm 1$). From these, *WMAP* measures the age of the universe ($t_0 = 13.7 \pm 0.2 \text{ Gyr}$) to an accuracy of $\sim 1\%$ by determining the CMB light travel time over the distance determined by the decoupling surface ($d_A = 14.0_{-0.3}^{+0.2} \text{ Gpc}$) and the geometry of the universe (i.e., flat). The age of the universe is also estimated via stars in three ways:

1. The main-sequence turnoff in globular clusters yielding a cluster age of $12 \pm 1 \text{ Gyr}$ (Reid 1997).
2. The temperature of the coldest white dwarfs in globular clusters yielding a cluster age of $12.7 \pm 0.7 \text{ Gyr}$ (Hansen et al. 2002).
3. Nucleosynthesis age dating yielding an age of $15.6 \pm 4.6 \text{ Gyr}$ (Cowan et al. 1999).

These stellar ages are all consistent with the age of the universe found by *WMAP*.

Matter density ($\Omega_m h^2$).—The matter density affects the height and shape of the acoustic peaks. The baryon-to-matter ratio determines the amplitude of the acoustic wave signal, and the matter-to-radiation ratio determines the epoch z_{eq} when the energy density of matter equaled the energy density of radiation. The amplitude of the early integrated Sachs-Wolfe effect signal is sensitive to the matter-radiation equality epoch. From these effects, *WMAP* measures the matter density $\Omega_m h^2$ to an accuracy of $\sim 5\%$. Large-scale structure observations measure $\Omega_m h$ through the shape of the power spectrum. When combined with estimates of h , this yields $\Omega_m h^2$. Large-scale velocity field measurements yield $\Omega_m^{0.6} b^{-1}$, where b is the bias in how the galaxy power spectrum traces the matter power spectrum [$P_{\text{gal}} = b^2 P(k)$]. Galaxy bispectrum measurements yield b , allowing for estimates of Ω_m . From the galaxy data, Verde et al. (2002) find $\Omega_m = 0.27 \pm 0.06$, which is consistent with the *WMAP* result of $\Omega_m = 0.27 \pm 0.04$.

Cluster lensing observations yield measurements of the total mass in the cluster. X-ray measurements give both the baryonic mass and the total mass through the gravitational potential. Sunyaev-Zeldovich effect observations give a different determination of the baryonic mass in clusters. The combined X-ray and Sunyaev-Zeldovich measurements give a value of $\Omega_b \Omega_m^{-1} = 0.081_{-0.011}^{+0.009} h^{-1}$ (Grego et al. 2001), which is reasonably consistent with 0.17 ± 0.01 from *WMAP*.

9.3. Implications for Inflation

WMAP data test several of the key predictions of the inflationary scenario (see Peiris et al. 2003 for further discussion):

1. Inflation predicts that the universe is flat. As noted in § 9.1 and discussed in detail in Spergel et al. (2003), the combination of *WMAP* data with either H_0 , Type Ia supernovae, or large-scale structure data constrains $|1 - \Omega_{\text{tot}}| < 0.03$.

2. Inflation predicts Gaussian random phase fluctuations. Komatsu et al. (2003) show that the CMB fluctuations have no detectable skewness and place strong constraints on primordial non-Gaussianity. Komatsu et al. (2003) also show that the Minkowski functionals of the *WMAP* data are consistent with the predictions of a model with Gaussian random phase fluctuations.

3. Inflation predicts fluctuations on scales that appear to be superhorizon scales in a Friedman-Robertson-Walker cosmology. The *WMAP* detection of an anticorrelation between polarization and temperature fluctuations on scales of $\sim 1^\circ - 2^\circ$ (Kogut et al. 2003) confirms this prediction and rules out subhorizon causal mechanisms for generating CMB fluctuations (Peiris et al. 2003).

4. Inflation predicts a nearly scale-invariant spectrum of fluctuations, as seen by *WMAP*.

The *WMAP* data, in combination with complementary cosmological data, not only test the basic ideas of the inflationary scenario but also rule out broad classes of inflationary models, and therefore the data guide us toward a specific workable inflationary scenario. The *WMAP* data place significant constraints on r , the tensor-to-scalar ratio, n_s , the slope of the scalar fluctuations, and $dn_s/d \ln k$, the scale dependence of these fluctuations. The addition of an admixture of isocurvature modes does not improve the *WMAP* model fits.

The best-fit model to the combination of the *WMAP*, ACBAR, CBI, 2dFGRS, and $\text{Ly}\alpha$ forest data has a spectral index that runs from $n > 1$ on the large scales probed by *WMAP* to $n < 1$ on the small scales probed by the 2dFGRS and the $\text{Ly}\alpha$ forest data. Only a handful of inflationary models predict this behavior. The Linde & Riotto (1997) hybrid inflationary model is one example. The data, however, do not yet require $n > 1$ on large scales: our best-fit model has $n_s = 1.03 \pm 0.04$ at $k = 0.002 \text{ Mpc}^{-1}$.

Our analysis of inflationary models (Peiris et al. 2003) marks the beginning of precision experimental tests of specific inflationary models. With the addition of ongoing *WMAP* observations and future improved analyses, *WMAP* will be able to more accurately constrain τ and hence n_s on large scales. When other CMB experiments are calibrated directly to the *WMAP* sky maps, they will provide improved measurements of the temperature angular power spectrum for $\ell > 700$. The upcoming release of the Sloan Digital Sky Survey (SDSS) power spectrum will provide an improved measurement of the galaxy power spectrum. The SDSS $\text{Ly}\alpha$ forest data are expected to be a significant improvement over the data used in our current analysis. Looking further toward the future, ESA's *Planck* mission will provide improved measurements of the CMB angular power spectrum on smaller angular scales and should be able to improve constraints on r .

10. DATA PRODUCTS

All of the *WMAP* data will be released. In addition, several ancillary and analyzed data sets are released. These include beam patterns, angular spectra, etc. Some software tools are also provided. An explanatory supplement provides detailed information about the *WMAP* in-flight operations and data products (Limon et al. 2003).¹² All *WMAP* data products are distributed through LAMBDA.¹³ This is a new NASA data center dedicated to the rapidly growing field of microwave background data archiving and analysis.

11. SUMMARY AND CONCLUSIONS

1. *WMAP* has produced high-quality full-sky maps in five widely separated frequency bands. These maps can be used to test cosmological models and serve as the primary legacy of the mission.

2. We have characterized and placed stringent limits on systematic measurement errors. The calibration is based on the modulation of the CMB dipole and is accurate to better than 0.5%.

3. We have demonstrated the ability to separate the CMB anisotropy from Galactic and extragalactic foregrounds. We provide masks for this purpose. In addition, we have produced CMB maps in which the Galactic signal is minimized.

4. We have a new determination of the dipole. It is $3.346 \pm 0.017 \text{ mK}$ in the direction

$$(l, b) = (263^\circ 85 \pm 0^\circ 1, 48^\circ 25 \pm 0^\circ 04) .$$

5. We have a new determination of the quadrupole amplitude. It is $Q_{\text{rms}} = 8 \pm 2 \mu\text{K}$, or $\Delta T_2^2 = 154 \pm 70 \mu\text{K}^2$.

6. We have placed tight new limits on the non-Gaussianity of the CMB anisotropy. The coupling coefficient of a quadratic non-Gaussian term is limited to $-58 < f_{\text{NL}} < 134$ (95% CL; Komatsu et al. 2003).

7. We have produced an angular power spectrum of the anisotropy with unprecedented accuracy and precision. The power spectrum is cosmic-variance-limited for $\ell < 354$, with a signal-to-noise ratio greater than 1 per mode to $\ell = 658$.

8. We have, for the first time, observed the angular power spectrum of temperature-polarization correlations with sufficient accuracy and precision to place meaningful limits on cosmology.

9. We have detected the epoch of reionization with an optical depth of $\tau = 0.17 \pm 0.04$. This implies a reionization epoch of $t_r = 180^{+220}_{-80} \text{ Myr}$ (95% CL) after the big bang at a redshift of $z_r = 20^{+10}_{-9}$ (95% CL) for a range of ionization scenarios. This early reionization is incompatible with the presence of a significant warm dark matter density.

10. We have fitted cosmological parameters to the data. We find results that are consistent with the big bang theory and inflation. We find that the addition of a running spectral index, while not required, improves the fit at the $\sim 2 \sigma$ level. We provide values and uncertainties for a host of parameters based on this non-power-law inflationary model. Our “best” values for cosmic parameters are given in Table 3.

¹² See

http://lambda.gsfc.nasa.gov/data/map/doc/WMAP_supplement.pdf.

¹³ See <http://lambda.gsfc.nasa.gov>.

11. *WMAP* continues to collect data and is currently approved for 4 years of operations at L2. The additional data, and more elaborate analyses, will help to further constrain models. The addition of other continuously improving CMB and large-scale structure observations is essential for progress toward the ultimate goal of a complete understanding of the global properties of the universe.

The *WMAP* mission is made possible by the support of the Office of Space Sciences at NASA Headquarters and by the hard and capable work of scores of scientists, engineers,

technicians, machinists, data analysts, budget analysts, managers, administrative staff, and reviewers. We are grateful to the National Radio Astronomy Observatory, which designed and produced the HEMT amplifiers that made *WMAP* possible. We are grateful to A. Riess for providing the likelihood surfaces for the supernova data. D. Finkbeiner supplied us with his full-sky composite map of $H\alpha$ emission in advance of publication. L. V. is supported by NASA through a Chandra fellowship issued by the Chandra X-Ray Observatory Center, operated by the Smithsonian Astrophysical Observatory. M. L. and G. T. are supported by the National Research Council.

REFERENCES

- Bahcall, N. A., Ostriker, J. P., Perlmutter, S., & Steinhardt, P. J. 1999, *Science*, 284, 1481
- Baker, J. C., et al. 1999, *MNRAS*, 308, 1173
- Barkana, R., Haiman, Z., & Ostriker, J. P. 2001, *ApJ*, 558, 482
- Barnes, C., et al. 2002, *ApJS*, 143, 567
- . 2003, *ApJS*, 148, 51
- Bennett, C. L., et al. 1992, *ApJ*, 396, L7
- . 1996, *ApJ*, 464, L1
- . 2003a, *ApJ*, 583, 1
- . 2003b, *ApJS*, 148, 97
- Benoit, A., et al. 2003, *A&A*, 399, L19
- Cen, R. 2003, *ApJ*, 591, 12
- Cheng, E. S., et al. 1997, *ApJ*, 488, L59
- Coble, K., et al. 1999, *ApJ*, 519, L5
- Cowan, J. J., Pfeiffer, B., Kratz, K.-L., Thielemann, F.-K., Sneden, C., Burles, S., Tytler, D., & Beers, T. C. 1999, *ApJ*, 521, 194
- Croft, R. A. C., Weinberg, D. H., Bolte, M., Burles, S., Hernquist, L., Katz, N., Kirkman, D., & Tytler, D. 2002, *ApJ*, 581, 20
- Dawson, K. S., Holzzapfel, W. L., Carlstrom, J. E., Joy, M., LaRoque, S. J., & Reese, E. D. 2001, *ApJ*, 553, L1
- de Bernardis, P., et al. 1994, *ApJ*, 422, L33
- de Oliveira-Costa, A., Devlin, M. J., Herbig, T., Miller, A. D., Netterfield, C. B., Page, L., & Tegmark, M. 1998, *ApJ*, 509, L77
- Dennison, B., Simonetti, J. H., & Topasna, G. A. 1998, *Publ. Astron. Soc. Australia*, 15, 147
- Dicker, S. R., et al. 1999, *MNRAS*, 309, 750
- D'Odorico, S., Dessauges-Zavadsky, M., & Molaro, P. 2001, *A&A*, 368, L21
- Finkbeiner, D. P. 2003, *ApJS*, 146, 407
- Finkbeiner, D. P., Davis, M., & Schlegel, D. J. 1999, *ApJ*, 524, 867
- Flett, A. M., & Henderson, C. 1979, *MNRAS*, 189, 867
- Freedman, W. L., et al. 2001, *ApJ*, 553, 47
- Ganga, K., Cheng, E., Meyer, S., & Page, L. 1993, *ApJ*, 410, L57
- Gaustad, J. E., McCullough, P. R., Rosing, W., & Buren, D. V. 2001, *PASP*, 113, 1326
- Górski, K. M., Banday, A. J., Bennett, C. L., Hinshaw, G., Kogut, A., Smoot, G. F., & Wright, E. L. 1996, *ApJ*, 464, L11
- Gott, J. R. I., Park, C., Juszkiewicz, R., Bies, W. E., Bennett, D. P., Bouchet, F. R., & Stebbins, A. 1990, *ApJ*, 352, 1
- Grainge, K., et al. 2003, *MNRAS*, 341, L23
- Grego, L., Carlstrom, J. E., Reese, E. D., Holder, G. P., Holzzapfel, W. L., Joy, M. K., Mohr, J. J., & Patel, S. 2001, *ApJ*, 552, 2
- Gundersen, J. O., et al. 1995, *ApJ*, 443, L57
- Halverson, N. W., et al. 2002, *ApJ*, 568, 38
- Hanany, S., et al. 2000, *ApJ*, 545, L5
- Hancock, S., Gutiérrez, C. M., Davies, R. D., Lasenby, A. N., Rocha, G., Rebolo, R., Watson, R. A., & Tegmark, M. 1997, *MNRAS*, 289, 505
- Hansen, B. M. S., et al. 2002, *ApJ*, 574, L155
- Harrison, D. L., et al. 2000, *MNRAS*, 316, L24
- Haslam, C. G. T., Klein, U., Salter, C. J., Stoffel, H., Wilson, W. E., Cleary, M. N., Cooke, D. J., & Thomasson, P. 1981, *A&A*, 100, 209
- Hinshaw, G., Banday, A. J., Bennett, C. L., Górski, K. M., Kogut, A., Lineweaver, C. H., Smoot, G. F., & Wright, E. L. 1996a, *ApJ*, 464, L25
- Hinshaw, G., Banday, A. J., Bennett, C. L., Górski, K. M., Kogut, A., Smoot, G. F., & Wright, E. L. 1996b, *ApJ*, 464, L17
- Hinshaw, G. F., et al. 2003a, *ApJS*, 148, 135
- . 2003b, *ApJS*, 148, 63
- Hivon, E., Górski, K. M., Netterfield, C. B., Crill, B. P., Prunet, S., & Hansen, F. 2002, *ApJ*, 567, 2
- Jarosik, N., et al. 2003a, *ApJS*, 145, 413
- . 2003b, *ApJS*, 148, 29
- Knox, L., & Page, L. 2000, *Phys. Rev. Lett.*, 85, 1366
- Kogut, A., Banday, A. J., Bennett, C. L., Górski, K. M., Hinshaw, G., Smoot, G. F., & Wright, E. L. 1996a, *ApJ*, 464, L5
- Kogut, A., Banday, A. J., Bennett, C. L., Górski, K. M., Hinshaw, G., Smoot, G. F., & Wright, E. L. 1996b, *ApJ*, 464, L29
- Kogut, A., et al. 1992, *ApJ*, 401, 1
- . 1996c, *ApJ*, 470, 653
- . 2003, *ApJS*, 148, 161
- Komatsu, E., & Spergel, D. N. 2001, *Phys. Rev. D*, 63, 63002
- Komatsu, E., et al. 2003, *ApJS*, 148, 119
- Kosowsky, A., & Turner, M. S. 1995, *Phys. Rev. D*, 52, 1739
- Kovac, J., et al. 2002, *Nature*, 420, 772
- Kuo, C. L., et al. 2002, *ApJ*, submitted (astro-ph/0212289)
- Leitch, E. M., Readhead, A. C. S., Pearson, T. J., Myers, S. T., Gulkis, S., & Lawrence, C. R. 2000, *ApJ*, 532, 37
- Limon, M., et al. 2003, *Wilkinson Microwave Anisotropy Probe (WMAP): Explanatory Supplement (Greenbelt: GSFC)*
- Linde, A. D., & Riotto, A. 1997, *Phys. Rev. D*, 56, 1841
- Mather, J. C., Fixsen, D. J., Shafer, R. A., Mosier, C., & Wilkinson, D. T. 1999, *ApJ*, 512, 511
- Mather, J. C., et al. 1990, *ApJ*, 354, L37
- Mauskopf, P. D., et al. 2000, *ApJ*, 536, L59
- Miller, A. D., et al. 1999, *ApJ*, 524, L1
- Minkowski, H. 1903, *Math. Ann.*, 57, 447
- Moore, B., Governato, F., Quinn, T., Stadel, J., & Lake, G. 1998, *ApJ*, 499, L5
- Myers, S. T., Readhead, A. C. S., & Lawrence, C. R. 1993, *ApJ*, 405, 8
- Netterfield, C. B., Devlin, M. J., Jarosik, N., Page, L., & Wollack, E. J. 1997, *ApJ*, 474, 47
- Oh, S. P., Spergel, D. N., & Hinshaw, G. 1999, *ApJ*, 510, 551
- O'Meara, J. M., Tytler, D., Kirkman, D., Suzuki, N., Prochaska, J. X., Lubin, D., & Wolfe, A. M. 2001, *ApJ*, 552, 718
- Padin, S., et al. 2001, *ApJ*, 549, L1
- Page, L., et al. 2003a, *ApJ*, 585, 566
- . 2003b, *ApJS*, 148, 39
- . 2003c, *ApJS*, 148, 233
- Pearson, T. J., et al. 2003, *ApJ*, 591, 556
- Peebles, P. J. E. 1984, *ApJ*, 284, 439
- Peiris, H., et al. 2003, *ApJS*, 148, 213
- Penzias, A. A., & Wilson, R. W. 1965, *ApJ*, 142, 419
- Percival, W. J., et al. 2001, *MNRAS*, 327, 1297
- Peterson, J. B., et al. 2000, *ApJ*, 532, L83
- Pettini, M., & Bowen, D. V. 2001, *ApJ*, 560, 41
- Piccirillo, L., et al. 1997, *ApJ*, 475, L77
- Reid, I. N. 1997, *AJ*, 114, 161
- Reynolds, R. J., Haffner, L. M., & Madsen, G. J. 2002, in *ASP Conf. Ser.* 282, *Galaxies: The Third Dimension*, ed. M. Rosado, L. Binette, & L. Arias (San Francisco: ASP), 31
- Ricotti, M. 2002, *MNRAS*, submitted (astro-ph/0212146)
- Riess, A. G., et al. 2001, *ApJ*, 560, 49
- Romeo, G., Ali, S., Femenia, B., Limon, M., Piccirillo, L., Rebolo, R., & Schaefer, R. 2001, *ApJ*, 548, L1
- Ruhl, J. E., et al. 2003, *ApJ*, submitted (astro-ph/0212229)
- Schlegel, D. J., Finkbeiner, D. P., & Davis, M. 1998, *ApJ*, 500, 525
- Smoot, G. F., et al. 1992, *ApJ*, 396, L1
- Spergel, D. N., & Steinhardt, P. J. 2000, *Phys. Rev. Lett.*, 84, 3760
- Spergel, D. N., et al. 2003, *ApJS*, 148, 175
- Tucker, G. S., Griffin, G. S., Nguyen, H. T., & Peterson, J. B. 1993, *ApJ*, 419, L45
- Tucker, G. S., Gush, H. P., Halpern, M., Shinkoda, I., & Towlson, W. 1997, *ApJ*, 475, L73
- Verde, L., et al. 2002, *MNRAS*, 335, 432
- . 2003, *ApJS*, 148, 195
- Wilson, G. W., et al. 2000, *ApJ*, 532, 57
- Wright, E. L., Bennett, C. L., Górski, K., Hinshaw, G., & Smoot, G. F. 1996a, *ApJ*, 464, L21
- Wright, E. L., Hinshaw, G., & Bennett, C. L. 1996b, *ApJ*, 458, L53
- Wright, E. L., et al. 1992, *ApJ*, 396, L13